nature chemical biology

Article

https://doi.org/10.1038/s41589-025-01925-0

Phase separation instead of binding strength determines target specificities of MAGUKs

Received: 17 December 2024

Accepted: 29 April 2025

Published online: 10 June 2025



Check for updates

Yan Chen 12,3,4, Chenxue Ma^{2,4}, Zeyu Shen 12, Shiwen Chen 12. Shihan Zhu $\mathbb{D}^{1,2}$, Bowen Jia $\mathbb{D}^{1,2}$, Shangyu Dang \mathbb{D}^2 & Mingjie Zhang $\mathbb{D}^1 \boxtimes$

Homologous proteins often have distinct functions, even if they share overlapping binding targets. PSD-95 and MAGI-2, two membrane-associated guanylate kinase (MAGUK)-family scaffolds in neuronal synapses, exemplify this. With unknown mechanisms, the two MAGUKs are localized at distinct subsynaptic compartments with PSD-95 inside the postsynaptic density (PSD) and MAGI-2 outside. Here we demonstrate that MAGI-2 forms condensates through phase separation. When coexisting with PSD proteins, the MAGI-2 condensate can enrich the extrasynaptic N-cadherin-β-catenin adhesion complex and the MAGI-2 condensates are immiscible with the PSD-95 condensates. Surprisingly, phosphorylated SAPAP is selectively enriched in the PSD-95 condensate, even though it binds to MAGI-2 with a higher affinity. The specific localization of SAPAP is because of the higher network complexities of the PSD-95-containing condensate than the MAGI-2 condensate. Thus, phase-separation-mediated molecular condensate formation can generate a previously unrecognized mode of molecular interaction and subcellular localization specificities that do not occur in dilute solutions.

Specific and regulated molecular interactions are the foundations of all cellular physiological processes. Textbooks taught us that, amid multiple binding targets with comparable concentrations, a protein preferentially binds to a target with the strongest binding affinity, unless this target is physically separated from the protein by physical barriers such as lipid membranes. Such binding competition equilibrium theory has been guiding biomolecular interaction studies both in vitro and in living cells and organisms and serves as a principle for selecting specific molecular interactions as drug targets. Using neuronal synapses as a paradigm, we demonstrate in this study that phase-separation-mediated formation of biological condensates can fundamentally change the biomolecular interaction specificities predicted by the classical binding competition equilibrium theory. We further provide a mechanistic explanation as to why such emergent property can occur upon forming biological condensates.

Neuronal synapses are highly compartmentalized signaling apparatuses that can undergo dynamic structural and molecular organization changes in response to stimulations. For example, the majority of excitatory synapses form submicron-sized postsynaptic protrusions on dendritic spines and a presynaptic bouton with a matching size closely opposes each spine^{1,2}. Synaptic adhesion molecules such as N-cadherins, neurexins and neuroligins have critical roles in aligning the presynaptic and postsynaptic compartments to ensure proper signal transmission speed and strength initiated by presynaptic released neurotransmitters²⁻¹¹. On the postsynaptic side, glutamate receptors are clustered in high densities by a group of scaffold proteins (Fig. 1a), including the DLG-family membrane-associated guanylate kinases (MAGUKs, represented by PSD-95) and its downstream proteins such as SAPAP, Shank and Homer^{12–15}. These scaffold proteins, together with glutamate receptors, form dense and large molecular assemblies networks through specific and multivalent interaction and through phase separation 16-20. Such glutamate-receptor-containing postsynaptic molecular assemblies form dense thickenings under the electron microscope and are known as postsynaptic densities

School of Life Sciences, Southern University of Science and Technology, Shenzhen, China. 2Division of Life Science, Hong Kong University of Science and Technology, Hong Kong, China. ³Greater Bay Biomedical Innocenter, Shenzhen Bay Laboratory, Shenzhen, China. ⁴These authors contributed equally: Yan Chen, Chenxue Ma. e-mail: zhangmj@sustech.edu.cn

(PSDs)^{1,21-24}. In addition to being enriched and clustered within the PSD, a portion of glutamate receptors are distributed on the plasma membranes outside but near the PSD and these population of receptors are referred to as extrasynaptic glutamate receptors²⁵⁻²⁷. Glutamate receptors can be dispersed from the PSD to extrasynaptic plasma membranes or, reversely, integrated into the PSD from extrasynaptic plasma membranes. Such subsynaptic compartmentalized distributions of neurotransmitter receptors and their dynamic redistributions are critical for stimulation-induced synaptic strength changes (that is, synaptic plasticity)²⁸⁻³⁵.

MAGI-2 (also known as synaptic scaffolding molecule) is another MAGUK scaffold protein known to exist in the postsynaptic compartment of excitatory synapses at high abundance 14,36,37. In addition to a defining guanylate kinase-like (GK) domain, all MAGUKs contain multiple PDZ domains 4 (Fig. 1b and Extended Data Fig. 1). Because of their similarities in domain organizations, PSD-95 and MAGI-2 share many overlapping binding synaptic proteins such as SAPAP 37,38, AMPA receptor (AMPAR) auxiliary subunit Stargazin (Stg) 18,39, N-methyl-p-aspartate receptors (NMDARs) 37,40-42 and neuroligins 8,41,43. Both PSD-95 and MAGI-2 have critical roles in synaptic functions including regulating synaptic development and AMPAR concentrations in synapses 7,12,36,44-48.

An intriguing observation is that, despite their structural similarities and capacities in binding to many common target proteins, MAGI-2 and PSD-95 have distinct subcompartmental localizations within dendritic spines. Biochemical fractionation, immuno-gold labeling coupled with electron microscopy and super-resolution optical microscopy studies all showed that PSD-95 is a core component of the PSD⁴⁹⁻⁵⁷. In sharp contrast, mass spectrometry and immunoblot analyses showed that biochemically purified PSDs are devoid of MAGI-2 (refs. 37,54,57). Given that MAGI-2 can directly bind to AMPAR auxiliary subunit Stg and regulate surface AMPAR level in spines³⁹, one may envision that MAGI-2 is localized in the extrasynaptic subcompartment and binds to AMPARs and/or other proteins that are dispersed from or to be integrated into the PSD. A puzzling question is how can the two similar MAGUK scaffold proteins exist in distinct subcompartments within tiny dendritic spine protrusions typically with a diameter of <0.5 μm. A more general question is why many homologous proteins have distinct functions even if they share similar target-binding properties.

We discover in this study that MAGI-2 and PSD-95 can organize distinct molecular assemblies through phase separation. The PSD core condensates organized by PSD-95 are immiscible with a molecular condensate formed by the MAGI-2–N-cadherin– β -catenin complex. The phase-in-phase organization of the PSD-95 and MAGI-2 organized condensates recapitulates the subsynaptic compartmentalized organization of the PSD core with respect to the extrasynaptic molecular assemblies. Most importantly, phase-separation-mediated biological condensate formation allows PSD-95 to selectively enrich SAPAP into the PSD condensate even though PSD-95 binds to SAPAP with a weaker

affinity than MAGI-2. Thus, the formation of condensates can define unique cellular spatial localizations of proteins that are not possible in homogeneous solutions. This emergent property of biological condensates will have broad implications for understanding the functions of biomolecules in general and for designing strategies in targeting biomolecules for translational purposes.

Results

MAGI-2 and PSD-95 are localized in distinct subsynaptic compartments

We first investigated subcellular distributions of the two MAGUKs in rat brains using differential centrifugations coupled with detergent extractions (Extended Data Fig. 2a). In such fractionation studies, MAGI-2 was recovered from synaptosomes and synaptic membrane factions but showed little abundance in the detergent-insoluble pellet fraction known as the PSD. In contrast, PSD-95, together with SAPAP, the GluA1 subunit of AMPAR and the GluN2B subunit of NMDAR, was enriched in the detergent-insoluble PSD fraction (Fig. 1c,d and Extended Data Fig. 2b). This biochemical fractionation result is consistent with findings from cellular fractionation and proteomic studies showing that PSD-95 mainly exists in the PSD and MAGI-2 does not localize in the PSD^{37,58,59}.

Fluorescence microscopic imaging studies showed that MAGI-2, either endogenous or overexpressed, is also enriched in the spines of synapses³⁶ (Fig. 1e). However, the resolution limit of conventional fluorescence microscopy could not provide subsynaptic localization information for the two MAGUKs. We next investigated the localizations of MAGI-2 and PSD-95 in the synapses using super-resolution fluorescence microscopy. Because the available antibodies of MAGI-2 are not suitable for the super-resolution imaging study of endogenous proteins, we knocked down endogenous MAGI-2 in rat neurons and rescued it with Flag-tagged MAGI-2. Using stochastic optical reconstruction microscopy (STORM) super-resolution imaging, we found that MAGI-2 and PSD-95 are in different subsynaptic compartments, with PSD-95 preferentially localized at the center regions beneath the postsynaptic membranes (Fig. 1e). We calculated the overlap coefficient of PSD-95 and MAGI-2 clusters to quantify the degree of colocalization. The degree of overlap between PSD-95 and MAGI-2 was lower than that between pairs of PSD scaffold proteins (Fig. 1e,f). Thus, MAGI-2 forms nanoclusters and is localized at more peripheral regions near the PSD-95 clusters. Together with the biochemical PSD fractionation results, we conclude that MAGI-2 is mainly localized outside the PSD and functions as an extrasynaptic scaffold protein.

MAGI-2 and PSD-95 organize synaptic protein condensates

We compared the quantitative binding affinities of MAGI-2 and PSD-95 in binding to Stg using isothermal titration calorimetry (ITC). For this assay and the remaining biochemical assays, we purified the full-length

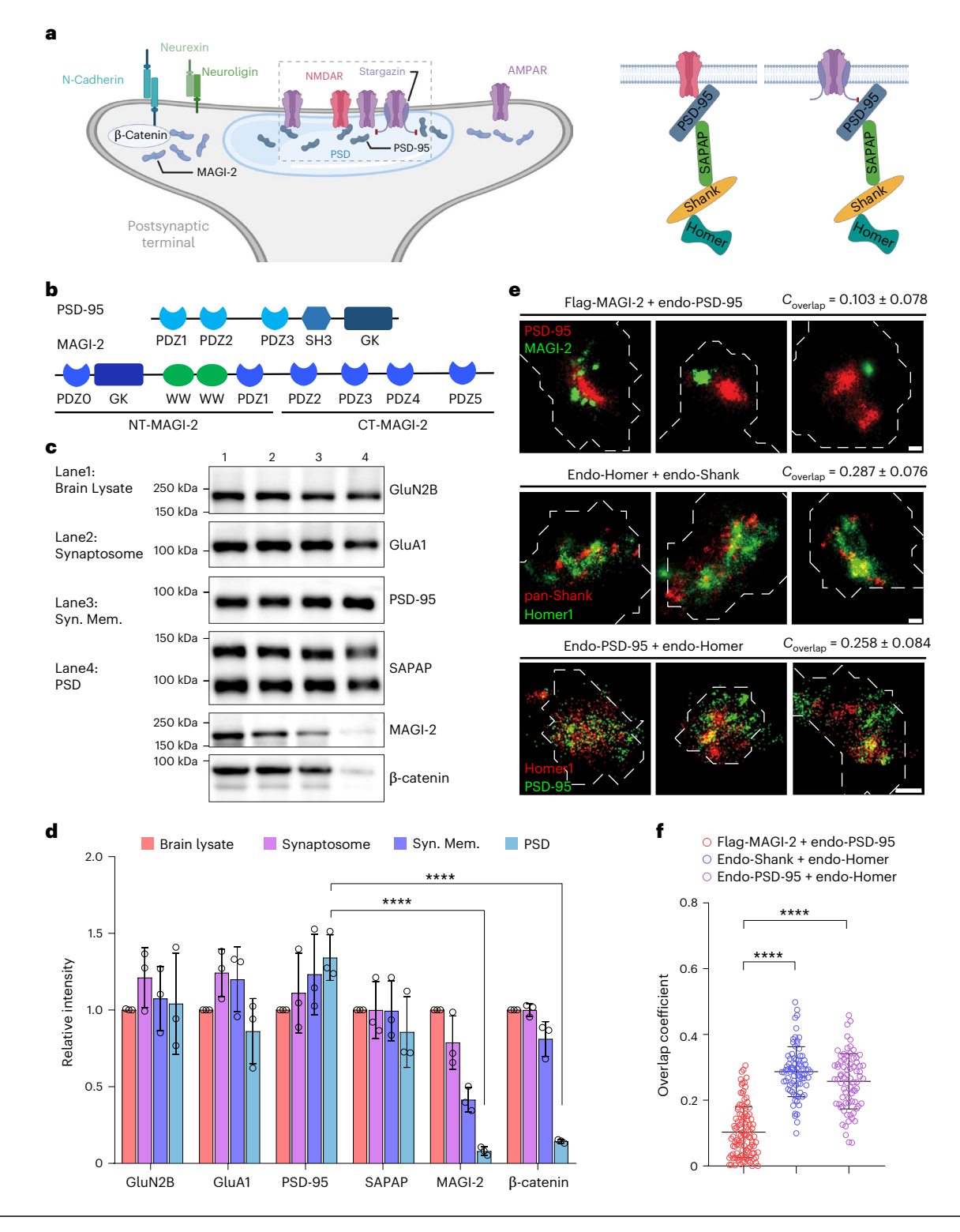
Fig. 1 | PSD-95 and MAGI-2 are localized in distinct subsynaptic compartments in neurons from rat brains. a, Left: overview scheme of postsynapse shows the cellular locations of PSD proteins and condensates. Right: zoomed-in view of the boxed region in the left scheme shows the interaction network of PSD scaffold proteins. Created with BioRender.com. b, Schematic diagrams of the domain organizations of MAGI-2 and PSD-95. MAGI-2 and PSD-95 contain multiple PDZ domains and a phosphoprotein-binding GK domain. The PDZO and GK domains of MAGI-2 form a structural supramodule. c, Representative western blot images showing subcellular localizations of MAGI-2, PSD-95 and a selected panel of other postsynaptic proteins in different fractions in the PSD fractionation experiments. Syn. Mem., synaptic membrane. d, Quantification of the PSD fractionation experiments showing distributions of the probed proteins in three batches of fractionation experiments. Unlike GluN2B, PSD-95 and SAPAP, very little MAGI-2 and β -catenin exist in the PSD fraction. Data represent the mean values \pm s.d. (n = 3 independent experiments). Statistical analysis was conducted using a two-way analysis of variance followed by Tukey's test. ****P < 0.0001.

e, STORM imaging showing distributions of Flag-tagged MAGI-2 and endogenous PSD-95 in rat hippocampal pyramidal neurons. As the control, STORM imaging was used to probe localizations of endogenous Homer 1 and Shank. White dashed lines demarcate the synaptic boundaries generated from the GFP signal. Homer 1 and Shank clusters overlap extensively. In contrast, the PSD-95 clusters and MAGI-2 clusters display very little overlap. The data showing the localization and overlap coefficient of PSD-95 and Homer were reanalyzed from a previous study ⁶⁸. Calculated overlap coefficient ($C_{\rm overlap}$) for each group is marked at the top of each row and expressed as average ± s.d. Scale bar, 100 nm. **f**, Scatter plot showing the quantification of data described in **d**. The calculated overlap coefficients were used to measure the degrees of overlaps between postsynaptic scaffolds. Data represent the mean values ± s.d. (n = 107, 78 and 77 individual synapses for MAGI-2 + PSD-95, Shank + Homer and PSD-95 + Homer, respectively, from three independent experiments). Statistical analysis was conducted using a two-tailed t-test. *****P< 0.0001.

MAGI-2 and its N-terminal or C-terminal fragments (Fig. 1b and Extended Data Fig. 3a) to high purity. Preparations of the full-length PSD-95, the entire cytoplasmic tail of Stg (Stg_CT) and the rest of the synaptic proteins were described in our earlier studies 17,18 . ITC assays showed that Stg_CT bound to NT-MAGI-2 with a $K_{\rm d}$ of ~2.65 μ M, whereas there was no detectable binding between Stg_CT and CT-MAGI-2 (Fig. 2a). Consistent with our earlier study 18 , full-length PSD-95 bound to Stg_CT with a $K_{\rm d}$ of ~0.56 μ M (Fig. 2a). Thus, both MAGI-2 and PSD-95 can bind to Stg CT, although MAGI-2 has a slightly lower affinity.

Our previous study showed that mixing PSD-95 and Stg_CT (each at $10~\mu\text{M}$, which is below their respective concentrations in synapses) led

to the formation of condensates through phase separation (Fig. 2b)¹⁸. Because MAGI-2 and PSD-95 share similar domain organization and bind to Stg_CT with comparable affinities, we asked whether MAGI-2 and Stg_CT can phase-separate in a test tube. When MAGI-2 and Stg_CT were mixed, they also phase-separated into condensates (Fig. 2b). As seen with the PSD-95-Stg_CT condensates, the MAGI-2-Stg_CT condensates could be dispersed by increasing salt concentrations in the assay buffer (Fig. 2c). As a scaffold protein, PSD-95 can organize the formation of the PSD condensates containing Stg_CT and key PSD scaffold proteins including GKAP (or SAPAP), Shank and Homer 3 (refs. 17,18) (Fig. 2d). We found that, like PSD-95, MAGI-2 could also



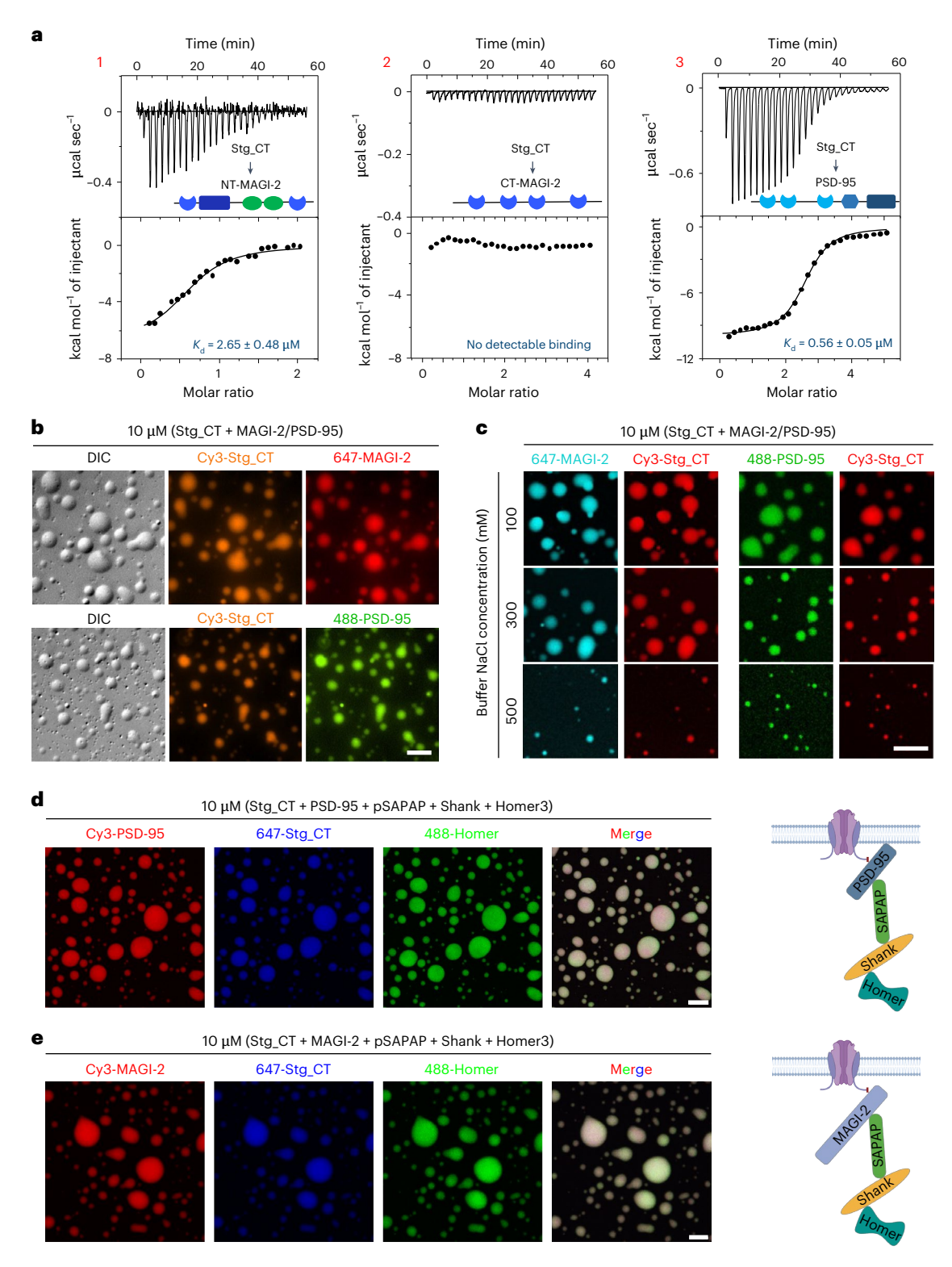


Fig. 2 | MAGI-2 and PSD-95 behave similarly in organizing postsynaptic density condensates. a, ITC-based measurements comparing the binding affinities of MAGI-2 fragments and PSD-95 to Stg_CT (aa 203–323): (1) 200 μM Stg_CT was titrated into 20 μM NT-MAGI-2; (2) 200 μM Stg_CT was titrated into 10 μM CT-MAGI-2; (3) 250 μM Stg_CT was titrated into 10 μM PSD-95. The fitted dissociation constants are shown in each panel. **b**, DIC and fluorescence images of 10 μM Alexa647-labeled full-length MAGI-2 or 10 μM Alexa488-labeled PSD-95 mixed with 10 μM Cy3–Stg_CT, showing the formation of condensates of the MAGI-2–Stg_CT and the PSD-95–Stg_CT mixtures through phase separation. Scale bar, 10 μm. **c**, Confocal images showing that the condensates

formed by PSD-95–Stg_CT and MAGI-2–Stg_CT complexes are sensitive to salt concentrations in the buffer. Scale bar, 10 $\mu m.$ **d**, Confocal images showing the formation of cocondensates composed of Stg_CT, PSD-95, pSAPAP, Shank and Homer. Right, scheme of the PSD-95 organized condensate. Scale bar, 10 $\mu m.$ **e**, Confocal images showing the formation of cocondensates composed of Stg_CT, MAGI-2, pSAPAP, Shank and Homer. Right: diagram showing that MAGI-2 can organize PSD condensate formation in vitro similarly to PSD-95. Scale bar, 10 $\mu m.$ The experiments in **b**-**e** were repeated three times independently with the same results. The schemes in **d**,**e** was created with BioRender.com.

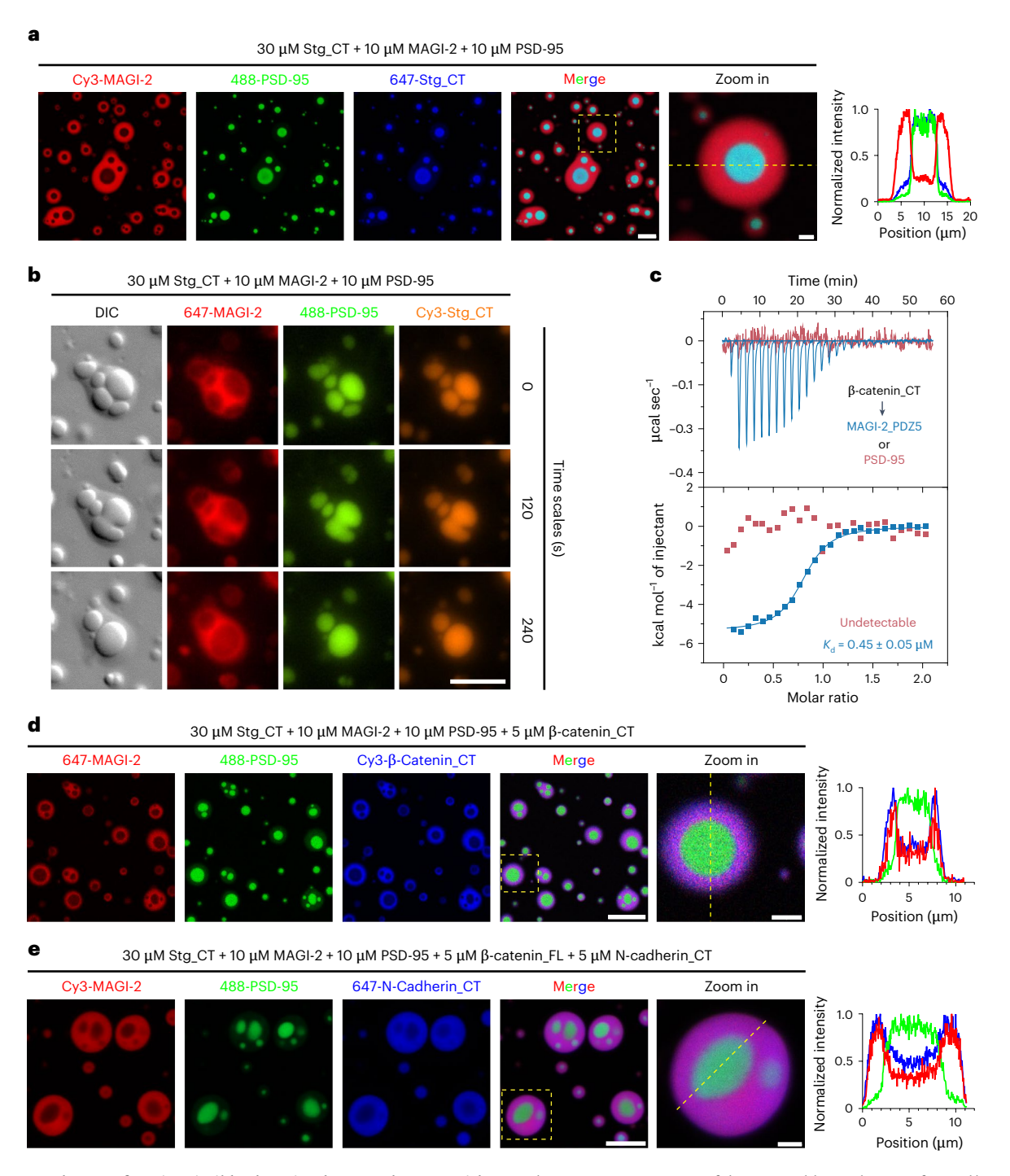


Fig. 3 | **MAGI-2** and **PSD-95** form immiscible phase-in-phase condensates with Stg_CT. a, Mixtures of 10 μM MAGI-2, 10 μM PSD-95 and 30 μM Stg_CT formed two immiscible condensed phases. MAGI-2 is in the outer compartment and PSD-95 is in the inner compartment. Stg_CT is preferentially enriched in the inner PSD-95 phase. Right: line scanning analysis of corresponding proteins in the selected droplet. Scale bars, 10 μm and 2 μm (zoomed-in view). **b**, Time-lapse DIC and fluorescence images showing fusions of the immiscible phase-separated condensates formed by MAGI-2, PSD-95 and Stg_CT. Scale bar, 10 μm. **c**, ITC-based experiments showing that MAGI-2 specifically binds to β-catenin_CT with a $K_{\rm d}$ of -0.45 μM. PSD-95 showed no detectable binding to β-catenin_CT. For ITC, 200 μM β-catenin_CT was titrated into 20 μM PSD-95 or 20 μM MAGI-2 PDZ5. **d**, β-catenin_CT shows colocalizations with MAGI-2

in the outer compartments of the immiscible condensates formed by 10 μM MAGI-2, 10 μM PSD-95, 30 μM Stg_CT and 5 μM β -catenin_CT. Right: line scanning analysis of the corresponding proteins in the selected droplet. Scale bars, 10 μm and 2 μm (zoomed-in view). e, N-cadherin_746–906 is selectively enriched in the MAGI-2- β -catenin condensate in the immiscible condensates formed by 10 μM MAGI-2, 10 μM PSD-95, 30 μM Stg_CT, 5 μM β -catenin_FL and 5 μM N-cadherin_746–906. Right: line scanning analysis of the corresponding proteins in the selected droplet. Scale bars, 10 μm and 2 μm (zoomed-in view). The experiments in a,b,d,e were repeated three times independently with the same results. The dashed box in a,d,e was selected for zoom-in and line-scanning analyses.

organize the formation of the same set of synaptic proteins into condensed droplets through phase separation (Fig. 2e). These results indicate that the two MAGUKs, MAGI-2 and PSD-95, share similar properties in binding to synaptic proteins and organizing these synaptic proteins into phase-separated condensates.

MAGI-2 and PSD-95 form immiscible condensates with Stg CT

We wondered whether phase separation might cause the two MAGUKs to form different condensates immiscible with each other as occurring in real synapses (Fig. 1e). To test this hypothesis, we mixed MAGI-2 and PSD-95 with Stg CT. To ensure that there was a sufficient amount of Stg CT for both MAGI-2 and PSD-95 to bind to, we included an excess amount of Stg CT in the mixtures (10 µM MAGI-2, 10 µM PSD-95 and 30 µM Stg CT: Fig. 3a,b), Strikingly, MAGI-2 and PSD-95 were found in two distinct condensates with a phase-in-phase organization. Stg CT was selectively enriched in the PSD-95 phase, although the MAGI-2 phase also contained a slightly higher concentration of Stg CT than the dilute solution (Fig. 3a,b). Differential interference contrast microscopy (DIC) imaging of the immiscible condensates showed that the MAGI-2 phase formed a ring-like structure encircling the PSD-95 droplets (Fig. 3b). The formed MAGI-2 and PSD-95 phases are liquid-like as the droplets in both phases underwent time-dependent fusions but the PSD-95 phase was never observed to fuse with the MAGI-2 phase (Fig. 3b). Next, we asked what would happen if we mixed other ligands with the two MAGUKs. Interestingly, the mixture of GluN2B tail (aa 1170-1482), MAGI-2 and PSD-95 also formed similar immiscible condensates (Extended Data Fig. 4). These results reveal that MAGI-2 and PSD-95 are distributed in distinct subcompartments upon forming immiscible condensates with Stg CT or GluN2B tail, which is reminiscent of the distinct subsynaptic distributions of the two MAGUKs in synapses (Fig. 1e).

MAGI-2 condensate recruits synaptic adhesion molecules

We next asked whether distinctly compartmentalized MAGI-2 might be able to recruit specific synaptic proteins. The β-catenin-N-cadherin complex is critical for transsynaptic alignments through homotypic cadherin-cadherin interactions^{7,60-62}. It is also known that the β-catenin–N-cadherin complex exists in clustered forms in the peripheral regions outside the PSD in spines. Genetic studies showed that mice with deletions of β-catenin and MAGI-2 share overlapping phenotypes^{10,63}. Additionally, β-catenin specifically binds to PDZ5 of MAGI-2 (refs. 64.65) (Fig. 3c) and there is no detectable binding between β-catenin and PSD-95 (Fig. 3c). The addition of the cytoplasmic tail of β -catenin (β -catenin_CT) to a mixture of MAGI-2, PSD-95 and Stg CT led to the specific recruitment of β-catenin CT into the MAGI-2 subcompartment without altering the PSD-95-Stg CT condensate formation (Fig. 3d). We further added purified cytoplasmic tail of N-cadherin to a mixture of MAGI-2, PSD-95, Stg CT and β-catenin mixture and found that N-cadherin CT is also specifically enriched in the MAGI-2 subcompartment (Fig. 3e). Using the in vitro biochemical reconstitution approach, we discovered a model for the distinct functions of the two MAGUK scaffold proteins in synapses, with PSD-95 organizing the PSD core protein complex containing AMPARs and MAGI-2 organizing synaptic β-catenin-N-cadherin adhesion complexes localized peripheral to the PSD.

Selective partitioning of pSAPAP to the PSD-95 condensates

SAPAPs are a family of abundant PSD proteins in synapses. It has been well established that the 14-residue repeat sequences (GK-binding repeats (GBRs)) in the N-terminal region of SAPAPs directly bind to the GK domain of PSD-95. In the absence of phosphorylation of a highly conserved serine in each of the repeat sequences, SAPAPs bind to PSD-95 with very low affinities (K_d of ~180 μ M) ^{66,67}. Phosphorylation of the conserved serine converts SAPAPs into strong PSD-95 binders (K_d of ~100 nM). MAGI-2 was one of the first proteins identified to bind to SAPAP (also known as GKAP) through its GK domain ³⁷. Thus, we

measured the binding affinity between SAPAP and MAGI-2 by ITC. We used CaMKII to fully phosphorylate the conserved serine residues in all three 14-residue repeats of SAPAP (denoted as pSAPAP) and found that pSAPAP binds to MAGI-2 with a $K_{\rm d}$ of ~26 nM (Fig. 4a,b). In parallel, we repeated our earlier finding that pSAPAP binds to PSD-95 with a $K_{\rm d}$ of ~180 nM (ref. 66), an affinity that is ~6–7-fold lower than binding to MAGI-2 (Fig. 4a). The full-length MAGI-2 readily formed condensates by itself and, thus, was not amenable to the ITC-based assay. As an alternative, we used a pulldown assay to confirm that the binding modes of full-length MAGI-2 and NT-MAGI-2 to pSAPAP were essentially the same (Extended Data Fig. 3b).

We next asked how pSAPAP might distribute in the two distinct PSD-95 and MAGI-2 condensates. We added pSAPAP into the MAGI-2, PSD-95 and Stg CT phase-in-phase mixtures. The addition of pSAPAP did not alter the compartmentalized organization of the two MAGUKs into distinct condensed phases (Fig. 4c). Remarkably, pSAPAP was selectively enriched in the PSD-95 condensates and the MAGI-2 condensates contained a very low amount of pSAPAP (Fig. 4c), even though MAGI-2 binds to pSAPAP with a higher affinity than PSD-95 (Fig. 4a). This finding is consistent with our earlier findings showing that, in synapses, phosphorylation of GKAP promotes its binding to PSD-95 and consequently promotes synaptogenesis^{67,68}. This finding is also consistent with the biochemical fractionation result showing that SAPAP is more enriched in the PSD-95-containing PSD core (Fig. 1c). The above results uncovered a totally unexpected property for proteins in condensed phase; phase-separation-mediated condensate formation can alter the binding specificity of a protein to its multiple competing target proteins, rendering their specific spatial localizations that cannot occur in dilute solutions. In this specific case, through forming distinct phase-separated condensates, pSAPAP is selectively enriched in the PSD-95-containing condensate by binding to PSD-95, although pSAPAP prefers to bind to MAGI-2 in dilute solutions (Fig. 4a,c).

Condensate network properties determine pSAPAP localization

What might be the underlying molecular mechanism governing the selective enrichment of pSAPAP in the PSD-95-containing condensate instead of the MAGI-2 condensate? Biological condensates exist as phase-separated and percolated molecular networks formed through multivalent molecular interactions^{69,70}. We recently demonstrated that both the network valency and network stability, manifested by binding affinities within each multivalent interaction network, can have a large impact on the mobilities and localization properties of molecules in condensates⁷¹. Thus we investigated whether the two MAGUKs, each in their own condensed phase, might have different network properties by single-molecule tracking (SMT) (Fig. 4d,e). Consistent with our earlier SMT studies⁶⁹, in the PSD-95 condensate containing Stg CT and PSD-95, proteins formed a more extensive percolated network such that PSD-95 existed in two major interexchanging motion states, with one in a network-confined state with very low mobility and the other in a freely diffusing state (Fig. 4e,f). In contrast, in the MAGI-2 condensates, MAGI-2 predominately existed in a freely diffusible state (Fig. 4d,f). The network property differences between the PSD-95-containing condensates and the MAGI-2-containing condensates likely originate from the unique multimerization properties of PSD-95 and MAGI-2. PSD-95 can form stable intermolecular oligomers⁷². As such, the PSD-95 condensate is highly branched and has a more complex network structure. In contrast, MAGI-2 does not form stable multimers; thus, the MAGI-2 condensate network is less branched.

If our above model stands, we predicted that changing the number of phosphorylation sites would alter the valency of phospho-SAPAP and thereby change its partition in the condensates organized by the two MAGUKs. To test this prediction, we generated SAPAP proteins with one, two and three GBRs phosphorylated (denoted as 1pi-SAPAP, 2pi-SAPAP and 3pi-SAPAP, respectively)⁶⁸. When comparing 1pi-SAPAP,

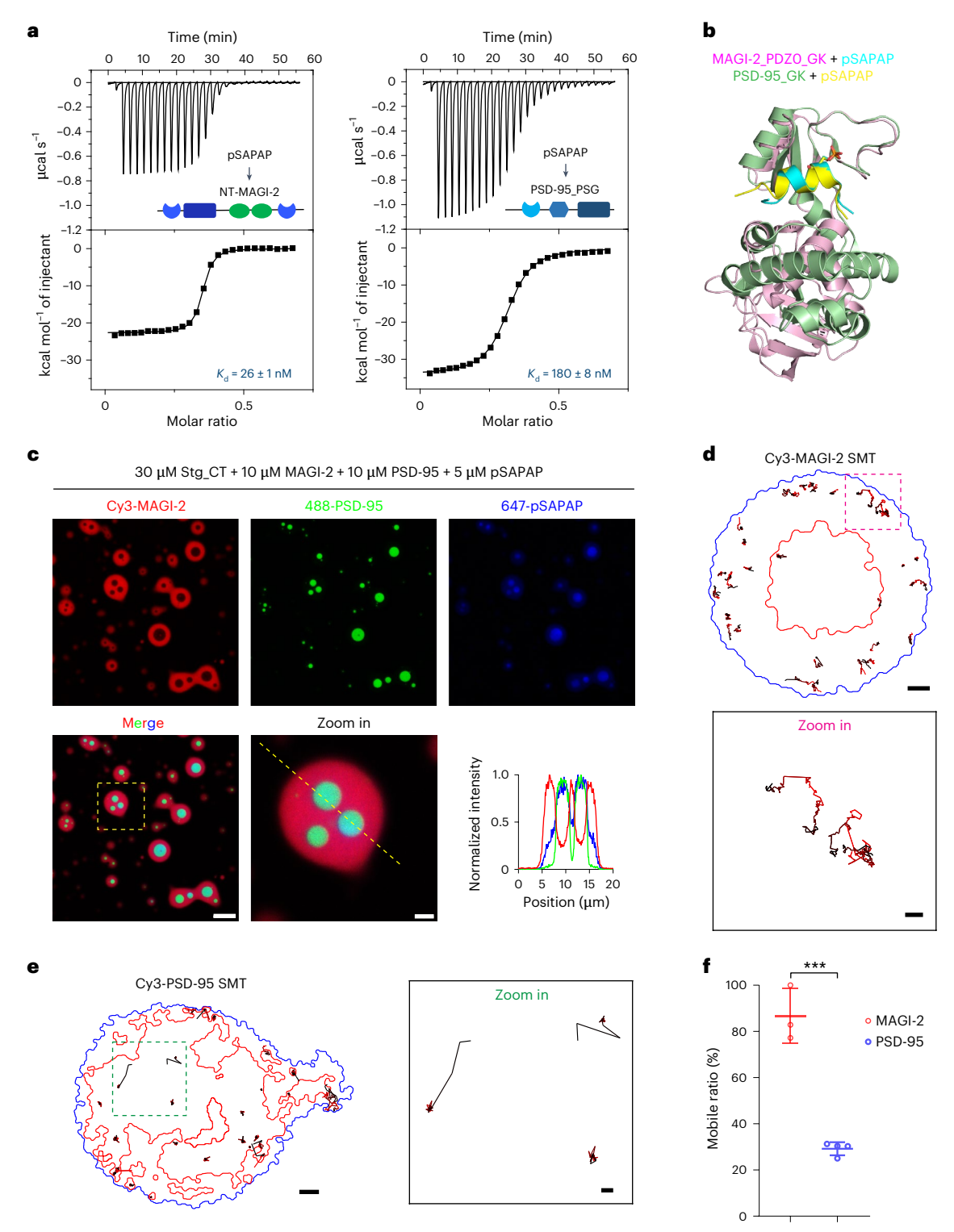


Fig. 4 | **Phosphorylated SAPAP is selectively partitioned into the PSD-95 phase. a**, ITC-based assays showing that pSAPAP binds to MAGI-2 (K_d of -26 nM) with a higher affinity than to PSD-95 (K_d of -180 nM). During the experiments, 100 μM pSAPAP was titrated into 30 μM NT-MAGI-2 or PSD-95_PSG. **b**, Alignment of the structures of the pSAPAP peptide-bound form of MAGI-2 PDZ0-GK (PDB 7YKH) and PSD-95 GK (PDB 5YPO) showing that the pSAPAP peptide binds to the GK domains from the two MAGUKs with a very similar mechanism. **c**, pSAPAP is selectively enriched in the PSD-95 condensate in the immiscible condensates formed by 10 μM MAGI-2, 10 μM PSD-95, 30 μM Stg_CT and 5 μM pSAPAP. Right: line scanning analysis of the corresponding proteins in the selected droplet. The experiment was repeated five times independently with the same results. Scale bars, 10 μm and 2 μm (zoomed-in views). The dashed box was selected for

zoom-in and line-scanning analyses. **d**, Super-resolution SMT of Cy3–MAGI-2 in the immiscible phases formed by 10 μ M MAGI-2, 10 μ M PSD-95 and 30 μ M Stg_CT. Representative trajectories of MAGI-2 molecules are shown. Scale bars, 200 nm (zoomed-in image) and 1 μ m (whole image). **e**, Super-resolution SMT of Cy3–PSD-95 in the immiscible phases formed by 10 μ M MAGI-2, 10 μ M PSD-95 and 30 μ M Stg_CT. Representative trajectories of PSD-95 molecules are plotted. Scale bars, 200 nm (zoomed-in image) and 1 μ m (whole image). **f**, Quantification of the mobile fractions of PSD-95 and MAGI-2 based on the SMT experiments described in **e**, **f**. A total of 4,063 and 3,436 trajectories for PSD-95 and MAGI-2 from three and four individual experiments, respectively, were used to perform this quantification. Data represent the mean values \pm s.d. Statistical analysis was conducted using a two-tailed t-test. ***P = 0.0002.

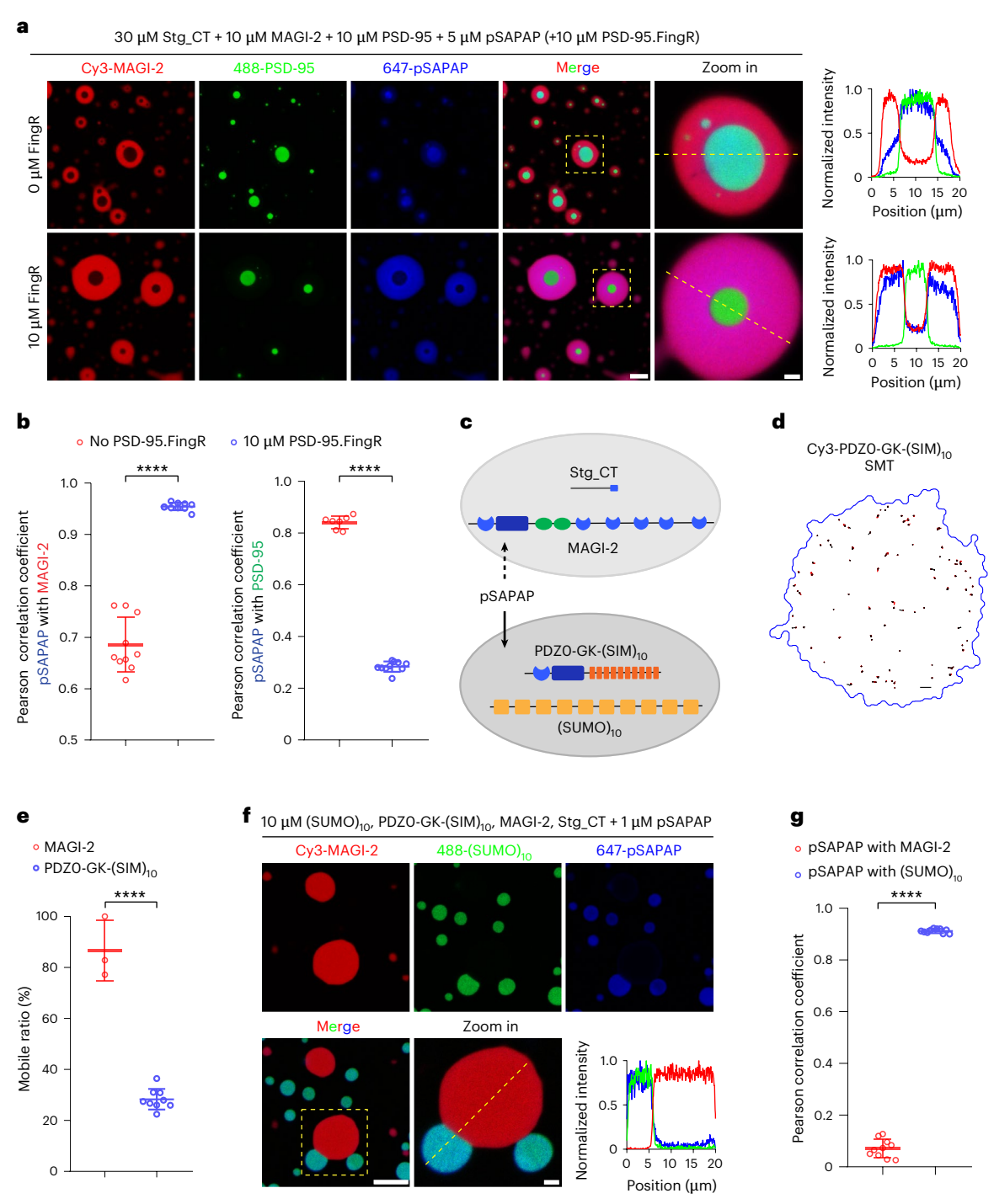


Fig. 5 | Blocking pSAPAP binding to PSD-95 or manipulating condensate network properties changes pSAPAP distribution. a, Blocking pSAPAP binding to PSD-95 by PSD-95. FingR resulted in pSAPAP dissociating from the PSD-95 condensate and becoming enriched in the MAGI-2 condensate. Right: line scanning analysis of the corresponding protein in the selected droplet. Scale bars, 10 μ m and 2 μ m (zoomed-in view). b, Quantification of the Pearson correlation coefficient (PCC) between pSAPAP and MAGI-2 and between pSAPAP and PSD-95 in the presence or absence of 10 μ M PSD-95. FingR. Data represent the mean values \pm s.d. Statistical analysis was conducted using a two-tailed t-test. ****P < 0.0001. c, Schematic diagram showing the design of the system to manipulate the pSAPAP distribution through condensate network complexity and stability. The PDZ0-GK domain was fused to the N-terminal end of (SIM)10, and (SIM)10 interacts with (SUMO)10 to form a highly percolated condensate. d, Super-resolution SMT of Cy3-PDZ0-GK-(SIM) $_{10}$ in the condensates formed by 10 μ M PDZ0-GK-(SIM) $_{10}$ and 10 μ M (SUMO) $_{10}$. Representative trajectories of

PDZ0-GK-(SIM) $_{10}$ molecules are plotted. Scale bar, 1 μ m. **e**, Quantification of the mobile fractions of PDZ0-GK-(SIM) $_{10}$ and MAGI-2 based on the SMT experiments described in **d** for the PDZ0-GK-(SIM) $_{10}$ -(SUMO) $_{10}$ condensate and the MAGI-2-Stg_CT condensate. A total of 4,063 and 6,655 trajectories for PDZ0-GK-(SIM) $_{10}$ and MAGI-2 from three and nine individual experiments, respectively, were used for the quantification. Data represent the mean values \pm s.d. Statistical analysis was conducted using a two-tailed t-test. ****P< 0.0001. **f**, pSAPAP was selectively enriched in the PDZ0-GK-(SIM) $_{10}$ condensate in the immiscible condensates formed by mixing 10 μ M each of PDZ0-GK-(SIM) $_{10}$, (SUMO) $_{10}$, MAGI-2 and Stg_CT. Bottom right: line scanning analysis of the corresponding proteins in the selected droplet. Scale bars, 10 μ m and 2 μ m (zoomed-in view). The dashed box in **a**, **f** was selected for zoom-in and line-scanning analyses. **g**, Quantification of the PCC values between pSAPAP and MAGI-2 and between pSAPAP and (SUMO) $_{10}$ described in **f**. Data represent the mean values \pm s.d. Statistical analysis was conducted using a two-tailed t-test. ****P<0.0001.

2pi-SAPAP and 3pi-SAPAP in our immiscible condensate system, we found that 1pi-SAPAP was enriched in the MAGI-2 condensate because of its stronger binding to MAGI-2 (Extended Data Fig. 5a). Despite also binding MAGI-2 with a higher affinity, 2pi-SAPAP became enriched in the PSD-95-containing condensate (Extended Data Fig. 5b). On the other hand, 3pi-SAPAP had the highest valency in binding to the MAGUKs. Satisfyingly, 3pi-SAPAP was strongly enriched in the PSD-95-containing condensate. The above results demonstrate that multivalent binding has an important role in defining the partition of protein-binding partners in the phase-separated system.

Manipulating pSAPAP distribution in immiscible condensates

We demonstrated that the apparent binding affinity of a protein to its target can be dramatically altered if the protein is anchored to a stable, percolated network formed in a condensate through phase separation ⁷¹. In this case, when PSD-95 is anchored in the stable and percolated PSD network, its apparent binding affinity or avidity for pSAPAP becomes substantially stronger. The binding affinity or avidity between MAGI-2 and pSAPAP should not differ too much when binding occurs in the dilute solution or in the MAGI-2 condensate. Consequently, when the PSD phase and MAGI-2 phase coexist, pSAPAP preferentially binds to PSD-95 and becomes enriched in the PSD phase.

The above analysis predicts that the network property differences of the two condensates can alter the binding avidities of pSAPAP to the MAGUKs. If this prediction is correct, we should be able to force pSA-PAP out of the PSD condensate by selectively blocking the binding of pSAPAP to PSD-95 and freed pSAPAP should then bind to MAGI-2, thus becoming enriched in the MAGI-2 phase. Identifying selective PSD-95 GK blockers without impacting MAGI-2 GK is not easy. We tested essentially all known natural cellular PSD-95 GK binders known to date and they were found to also bind to MAGI-2 with comparable affinities^{67,73}. Interestingly, a widely used intrabody known as PSD-95. FingR was developed to target PSD-95 in neurons and binds to PSD-95 with a high affinity74. We unexpectedly found that PSD-95. FingR binds to the phosphorylated SAPAP-binding pocket of PSD-95 GK and PSD-95. FingR can effectively block pSAPAP from binding to PSD-95. Most importantly, PSD-95.FingR is highly selective in binding to the DLG-family MAGUKs and the intrabody shows no detectable binding to MAGI-2. Satisfyingly, the addition of PSD-95. FingR to the MAGI-2, PSD-95, Stg CT and pSAPAP cocondensates led to a shift of pSAPAP from the PSD-95 condensate to the MAGI-2 condensate (Fig. 5a.b).

If preferential partitioning of pSAPAP to the PSD-95-containing PSD condensate instead of the MAGI-2 condensate is because of the stronger network property of the PSD condensate mainly driven by PSD-95, we predicted that we should be able to manipulate the pSAPAP targeting in immiscible condensates by engineering condensate network complexity and stability. To test this hypothesis, we took advantage of a synthetic multivalent condensate system composed of (SIM)₁₀ (ten tandem repeats of the SUMO interaction motif) and $(SUMO)_{10}$ (ref. 75). The $(SIM)_{10}$ - $(SUMO)_{10}$ condensate was completely immiscible from the MAGI-2-Stg_CT condensate (Extended Data Fig. 7b). We fused the PDZO-GK domain of MAGI-2 to the N-terminal end of (SIM)₁₀ and confirmed that the fusion protein formed a stable complex with pSAPAP (Fig. 5c and Extended Data Fig. 6a). The binding affinity between PDZO-GK-(SIM)₁₀ and pSAPAP was the same as that between NT-MAGI-2 and pSAPAP (Extended Data Fig. 6b). The PDZO-GK-(SIM)₁₀-(SUMO)₁₀ mixture formed a condensate that could robustly recruit pSAPAP (Extended Data Fig. 7a). As a control, the (SIM)₁₀-(SUMO)₁₀ condensate could not enrich pSA-PAP (Extended Data Fig. 7c,d). SMT experiments revealed that the PDZ0-GK-(SIM)₁₀-(SUMO)₁₀ condensate formed a highly percolated network as both PDZO-GK-(SIM)₁₀ and (SUMO)₁₀ in the condensate spent most of the time in the confined state with occasional switching to the mobile state (Fig. 5d,e and Extended Data Fig. 7e). In contrast, MAGI-2 in the MAGI-2-Stg CT condensate was largely mobile (Fig. 5e). When mixing pSAPAP with the PDZ0-GK-(SIM) $_{10}$ -(SUMO) $_{10}$ and the MAGI-2-Stg_CT condensates, the PDZ0-GK-(SIM) $_{10}$ -(SUMO) $_{10}$ condensate and the MAGI-2-Stg_CT condensate were totally immiscible (Fig. 5f). Remarkably, pSAPAP was selectively enriched into the PDZ0-GK-(SIM) $_{10}$ -(SUMO) $_{10}$ condensate and there was no pSAPAP enrichment in the MAGI-2-Stg_CT condensate (Fig. 5c,f,g). Thus, the selective enrichment of pSAPAP into the PDZ0-GK-(SIM) $_{10}$ -(SUMO) $_{10}$ condensate is because of its higher percolation than the MAGI-2-Stg_CT condensate.

Discussion

In this work, we discovered that two MAGUK synaptic scaffold proteins, PSD-95 and MAGI-2, can form two immiscible condensates through phase separation, each with a distinct set of proteins, even though the two scaffold proteins share common binding targets. The PSD-95-containing condensate corresponds to the PSD assemblies in the synapse and the MAGI-2-containing condensate corresponds to the extrasynaptic MAGI-2 condensate. Thus, our study provides a mechanistic explanation of why and how different MAGUKs are preferentially localized at distinct subsynaptic compartments and perform specific functions.

The most unexpected and important finding of the current study is that the formation of biological condensates through phase separation can alter the binding affinities or avidities of a protein to its different targets with respect to the corresponding binding modes measured in dilute solutions. Consequently, phase-separation-mediated condensate formation can generate cellular localization specificities of proteins that cannot occur in dilute solutions. In this study, phosphorylated SAPAP is preferentially enriched into the PSD-95-containing PSD condensate instead of the MAGI-2 condensate, even though pSAPAP has a higher binding affinity to MAGI-2 than to PSD-95. This preferential targeting of pSAPAP to the PSD-95-containing condensate is because the PSD condensate has higher network complexity and stability than the MAGI-2 condensate.

We recently demonstrated, using natural segregation of the excitatory PSD and inhibitory PSD as a paradigm, that formation of percolated PSD networks can disrupt a pair of very strong proteinprotein interactions with a K_d of ~4 nM measured in dilute solution⁷¹. The findings described in this study, together with those described in our recently studies^{69,71}, will have far-reaching implications for biomolecular interactions and subcellular localizations in living cells in general. We present a few such possibilities. First, binding affinities measured between a protein and its multiple targets in dilute solutions do not necessarily correctly predict their interactions in cells. The formation of biological condensates can alter their apparent binding affinities. Second, phase-separation-mediated formation of biological condensates can modify the binding specificities of a protein to its multiple targets as illustrated by the binding of pSAPAP to PSD-95 or to MAGI-2 in the current study or to the same PDZO-GK supramodule in native MAGI-2 or the PDZO-GK-(SIM)₁₀ chimera. Third, upon forming condensates, cellular localizations and dynamic behaviors of proteins are intimately linked to the network properties of the condensate; thus, it is possible to manipulate the cellular localization of a protein by targeting the molecular network in which this protein resides without directly targeting this protein. Such emergent properties of molecules in biological condensates could offer new opportunities for choosing molecular or even network targets for translational applications.

Online content

Any methods, additional references, Nature Portfolio reporting summaries, source data, extended data, supplementary information, acknowledgements, peer review information; details of author contributions and competing interests; and statements of data and code availability are available at https://doi.org/10.1038/s41589-025-01925-0.

References

- Harris, K. M. & Weinberg, R. J. Ultrastructure of synapses in the mammalian brain. Cold Spring Harb. Perspect. Biol. 4, a005587 (2012).
- Sudhof, T. C. The cell biology of synapse formation. J. Cell Biol. 220, e202103052 (2021).
- Aiga, M., Levinson, J. N. & Bamji, S. X. N-cadherin and neuroligins cooperate to regulate synapse formation in hippocampal cultures. J. Biol. Chem. 286, 851–858 (2011).
- Biederer, T., Kaeser, P. S. & Blanpied, T. A. Transcellular nanoalignment of synaptic function. Neuron 96, 680–696 (2017).
- Bruses, J. L. N-cadherin signaling in synapse formation and neuronal physiology. Mol. Neurobiol. 33, 237–252 (2006).
- Jiang, X., Sando, R. & Sudhof, T. C. Multiple signaling pathways are essential for synapse formation induced by synaptic adhesion molecules. *Proc. Natl Acad. Sci. USA* 118, e2000173118 (2021).
- Okuda, T., Yu, L. M., Cingolani, L. A., Kemler, R. & Goda, Y. β-Catenin regulates excitatory postsynaptic strength at hippocampal synapses. *Proc. Natl Acad. Sci. USA* 104, 13479–13484 (2007).
- Song, J. Y., Ichtchenko, K., Sudhof, T. C. & Brose, N. Neuroligin 1 is a postsynaptic cell-adhesion molecule of excitatory synapses. *Proc. Natl Acad. Sci. USA* 96, 1100–1105 (1999).
- Tanaka, H. et al. Molecular modification of N-cadherin in response to synaptic activity. Neuron 25, 93–107 (2000).
- Bamji, S. X. et al. Role of β-catenin in synaptic vesicle localization and presynaptic assembly. Neuron 40, 719–731 (2003).
- 11. Tang, A. H. et al. A trans-synaptic nanocolumn aligns neurotransmitter release to receptors. *Nature* **536**, 210–214 (2016).
- Chen, X. et al. PSD-95 family MAGUKs are essential for anchoring AMPA and NMDA receptor complexes at the postsynaptic density. Proc. Natl Acad. Sci. USA 112, E6983–E6992 (2015).
- Xu, W. PSD-95-like membrane associated guanylate kinases (PSD-MAGUKs) and synaptic plasticity. Curr. Opin. Neurobiol. 21, 306–312 (2011).
- Zhu, J., Shang, Y. & Zhang, M. Mechanistic basis of MAGUKorganized complexes in synaptic development and signalling. *Nat. Rev. Neurosci.* 17, 209–223 (2016).
- Elias, G. M. & Nicoll, R. A. Synaptic trafficking of glutamate receptors by MAGUK scaffolding proteins. *Trends Cell Biol.* 17, 343–352 (2007).
- Zeng, M. et al. Phase transition in postsynaptic densities underlies formation of synaptic complexes and synaptic plasticity. Cell 166, 1163–1175 (2016).
- Zeng, M. et al. Reconstituted postsynaptic density as a molecular platform for understanding synapse formation and plasticity. *Cell* 174, 1172–1187 (2018).
- Zeng, M. et al. Phase separation-mediated TARP/MAGUK complex condensation and AMPA receptor synaptic transmission. *Neuron* 104, 529–543 (2019).
- Hayashi, Y., Ford, L. K., Fioriti, L., McGurk, L. & Zhang, M. Liquid– liquid phase separation in physiology and pathophysiology of the nervous system. J. Neurosci. 41, 834–844 (2021).
- Chen, X., Wu, X., Wu, H. & Zhang, M. Phase separation at the synapse. Nat. Neurosci. 23, 301–310 (2020).
- Aoki, C. et al. Electron microscopic immunocytochemical detection of PSD-95, PSD-93, SAP-102, and SAP-97 at postsynaptic, presynaptic, and nonsynaptic sites of adult and neonatal rat visual cortex. Synapse 40, 239–257 (2001).
- 22. Chen, X. et al. PSD-95 is required to sustain the molecular organization of the postsynaptic density. *J. Neurosci.* **31**, 6329–6338 (2011).
- Chen, X. et al. Organization of the core structure of the postsynaptic density. *Proc. Natl Acad. Sci. USA* 105, 4453–4458 (2008).

- Harris, K. M., Jensen, F. E. & Tsao, B. Three-dimensional structure of dendritic spines and synapses in rat hippocampus (CA1) at postnatal day 15 and adult ages: implications for the maturation of synaptic physiology and long-term potentiation. *J. Neurosci.* 12, 2685–2705 (1992).
- 25. Kennedy, M. J., Davison, I. G., Robinson, C. G. & Ehlers, M. D. Syntaxin-4 defines a domain for activity-dependent exocytosis in dendritic spines. *Cell* **141**, 524–535 (2010).
- Soundarapandian, M. M. et al. Expression of functional Kir6.1 channels regulates glutamate release at CA3 synapses in generation of epileptic form of seizures. *J. Neurochem.* 103, 1982–1988 (2007).
- Tao-Cheng, J. H. et al. Trafficking of AMPA receptors at plasma membranes of hippocampal neurons. *J. Neurosci.* 31, 4834–4843 (2011).
- Penn, A. C. et al. Hippocampal LTP and contextual learning require surface diffusion of AMPA receptors. *Nature* **549**, 384–388 (2017).
- 29. Groc, L. & Choquet, D. Linking glutamate receptor movements and synapse function. *Science* **368**, eaay4631 (2020).
- Borgdorff, A. J. & Choquet, D. Regulation of AMPA receptor lateral movements. *Nature* 417, 649–653 (2002).
- Heine, M. et al. Surface mobility of postsynaptic AMPARs tunes synaptic transmission. Science 320, 201–205 (2008).
- 32. Huganir, R. L. & Nicoll, R. A. AMPARs and synaptic plasticity: the last 25 years. *Neuron* **80**, 704–717 (2013).
- MacGillavry, H. D., Song, Y., Raghavachari, S. & Blanpied, T. A. Nanoscale scaffolding domains within the postsynaptic density concentrate synaptic AMPA receptors. *Neuron* 78, 615–622 (2013).
- 34. Makino, H. & Malinow, R. AMPA receptor incorporation into synapses during LTP: the role of lateral movement and exocytosis. *Neuron* **64**, 381–390 (2009).
- Nishiyama, J. & Yasuda, R. Biochemical computation for spine structural plasticity. Neuron 87, 63–75 (2015).
- Danielson, E. et al. S-SCAM/MAGI-2 is an essential synaptic scaffolding molecule for the GluA2-containing maintenance pool of AMPA receptors. J. Neurosci. 32, 6967–6980 (2012).
- Hirao, K. et al. A novel multiple PDZ domain-containing molecule interacting with N-methyl-D-aspartate receptors and neuronal cell adhesion proteins. J. Biol. Chem. 273, 21105–21110 (1998).
- Kim, E. et al. GKAP, a novel synaptic protein that interacts with the guanylate kinase-like domain of the PSD-95/SAP90 family of channel clustering molecules. J. Cell Biol. 136, 669–678 (1997).
- Deng, F., Price, M. G., Davis, C. F., Mori, M. & Burgess, D. L. Stargazin and other transmembrane AMPA receptor regulating proteins interact with synaptic scaffolding protein MAGI-2 in brain. J. Neurosci. 26, 7875–7884 (2006).
- Iida, J. et al. Synaptic scaffolding molecule α is a scaffold to mediate N-methyl-D-aspartate receptor-dependent RhoA activation in dendrites. Mol. Cell. Biol. 27, 4388–4405 (2007).
- 41. Irie, M. et al. Binding of neuroligins to PSD-95. Science **277**, 1511–1515 (1997).
- 42. Sattler, R. et al. Specific coupling of NMDA receptor activation to nitric oxide neurotoxicity by PSD-95 protein. *Science* **284**, 1845–1848 (1999).
- 43. Iida, J., Hirabayashi, S., Sato, Y. & Hata, Y. Synaptic scaffolding molecule is involved in the synaptic clustering of neuroligin. *Mol. Cell Neurosci.* **27**, 497–508 (2004).
- 44. Elias, G. M. et al. Synapse-specific and developmentally regulated targeting of AMPA receptors by a family of MAGUK scaffolding proteins. *Neuron* **52**, 307–320 (2006).
- Bhattacharyya, S., Biou, V., Xu, W., Schluter, O. & Malenka, R. C. A critical role for PSD-95/AKAP interactions in endocytosis of synaptic AMPA receptors. *Nat. Neurosci.* 12, 172–181 (2009).

- Migaud, M. et al. Enhanced long-term potentiation and impaired learning in mice with mutant postsynaptic density-95 protein. Nature 396, 433–439 (1998).
- Schnell, E. et al. Direct interactions between PSD-95 and Stargazin control synaptic AMPA receptor number. Proc. Natl Acad. Sci. USA 99, 13902–13907 (2002).
- Ehrlich, I. & Malinow, R. Postsynaptic density 95 controls AMPA receptor incorporation during long-term potentiation and experience-driven synaptic plasticity. J. Neurosci. 24, 916–927 (2004).
- Cho, K. O., Hunt, C. A. & Kennedy, M. B. The rat brain postsynaptic density fraction contains a homolog of the *Drosophila* discs-large tumor suppressor protein. *Neuron* 9, 929–942 (1992).
- Dosemeci, A., Weinberg, R. J., Reese, T. S. & Tao-Cheng, J. H. The postsynaptic density: there is more than meets the eye. Front. Synaptic Neurosci. 8, 23 (2016).
- Funke, L., Dakoji, S. & Bredt, D. S. Membrane-associated guanylate kinases regulate adhesion and plasticity at cell junctions. *Annu. Rev. Biochem.* 74, 219–245 (2005).
- Kennedy, M. B. The postsynaptic density at glutamatergic synapses. *Trends Neurosci.* 20, 264–268 (1997).
- Sheng, M. & Hoogenraad, C. C. The postsynaptic architecture of excitatory synapses: a more quantitative view. *Annu. Rev. Biochem.* 76, 823–847 (2007).
- Vinade, L. et al. Affinity purification of PSD-95-containing postsynaptic complexes. J. Neurochem. 87, 1255–1261 (2003).
- Wilson, R. S. et al. Development of targeted mass spectrometry-based approaches for quantitation of proteins enriched in the postsynaptic density (PSD). *Proteomes* 7, 12 (2019).
- Li, J. et al. Spatiotemporal profile of postsynaptic interactomes integrates components of complex brain disorders. *Nat. Neurosci.* 20, 1150–1161 (2017).
- Zhou, J. et al. Proteomic analysis of postsynaptic density in Alzheimer's disease. Clin. Chim. Acta 420, 62–68 (2013).
- Cheng, D. et al. Relative and absolute quantification of postsynaptic density proteome isolated from rat forebrain and cerebellum. Mol. Cell Proteom. 5, 1158–1170 (2006).
- Roy, M. et al. Regional diversity in the postsynaptic proteome of the mouse brain. *Proteomes* 6, 31 (2018).
- Vitureira, N., Letellier, M., White, I. J. & Goda, Y. Differential control of presynaptic efficacy by postsynaptic N-cadherin and β-catenin. Nat. Neurosci. 15, 81–89 (2011).
- Mendez, P., De Roo, M., Poglia, L., Klauser, P. & Muller, D. N-cadherin mediates plasticity-induced long-term spine stabilization. J. Cell Biol. 189, 589–600 (2010).
- 62. Seong, E., Yuan, L. & Arikkath, J. Cadherins and catenins in dendrite and synapse morphogenesis. *Cell Adh. Migr.* **9**, 202–213 (2015).

- 63. Wickham, R. J. et al. Learning impairments and molecular changes in the brain caused by β -catenin loss. *Hum. Mol. Genet.* **28**, 2965–2975 (2019).
- Nishimura, W., Yao, I., Iida, J., Tanaka, N. & Hata, Y. Interaction of synaptic scaffolding molecule and β-catenin. J. Neurosci. 22, 757–765 (2002).
- 65. Zhang, H. et al. Phase separation of MAGI2-mediated complex underlies formation of slit diaphragm complex in glomerular filtration barrier. *J. Am. Soc. Nephrol.* **32**, 1946–1960 (2021).
- Zhu, J. et al. Guanylate kinase domains of the MAGUK family scaffold proteins as specific phospho-protein-binding modules. EMBO J. 30, 4986–4997 (2011).
- Zhu, J. et al. Synaptic targeting and function of SAPAPs mediated by phosphorylation-dependent binding to PSD-95 MAGUKs. Cell Rep. 21, 3781–3793 (2017).
- 68. Wu, H. et al. Phosphorylation-dependent membraneless organelle fusion and fission illustrated by postsynaptic density assemblies. *Mol. Cell* **84**, 309–326 (2024).
- 69. Shen, Z. et al. Biological condensates form percolated networks with molecular motion properties distinctly different from dilute solutions. *eLife* **12**, e81907 (2023).
- Mittag, T. & Pappu, R. V. A conceptual framework for understanding phase separation and addressing open questions and challenges. *Mol. Cell* 82, 2201–2214 (2022).
- Zhu, S. et al. Demixing is a default process for biological condensates formed via phase separation. Science 384, 920–928 (2024).
- Zeng, M., Ye, F., Xu, J. & Zhang, M. PDZ ligand binding-induced conformational coupling of the PDZ-SH3-GK tandems in PSD-95 family MAGUKs. J. Mol. Biol. 430, 69–86 (2018).
- Zhang, M. et al. Phosphorylation-dependent recognition of diverse protein targets by the cryptic GK domain of MAGI MAGUKs. Sci. Adv. 9, eadf3295 (2023).
- 74. Gross, G. G. et al. Recombinant probes for visualizing endogenous synaptic proteins in living neurons. *Neuron* **78**, 971–985 (2013).
- 75. Banani, S. F. et al. Compositional control of phase-separated cellular bodies. *Cell* **166**, 651–663 (2016).

Publisher's note Springer Nature remains neutral with regard to jurisdictional claims in published maps and institutional affiliations.

Springer Nature or its licensor (e.g. a society or other partner) holds exclusive rights to this article under a publishing agreement with the author(s) or other rightsholder(s); author self-archiving of the accepted manuscript version of this article is solely governed by the terms of such publishing agreement and applicable law.

© The Author(s), under exclusive licence to Springer Nature America, Inc. 2025

Methods

Bacterial strain

Escherichia coli BL21(DE3) cells (Agilent Technologies) were used in this study to produce recombinant proteins. Cells were cultured in Luria-Bertani (LB) medium supplemented with necessary antibiotics.

Animals

Embryonic day 19 rats (Sprague-Dawley) and adult 8-week-old mice (C57BL) were housed in groups of three to five per cage under a 12-hour light–dark cycle (lighting from 8:00 a.m. to 8:00 p.m.) with food and water available ad libitum, at a consistent ambient temperature (21 \pm 1 °C) and humidity (50% \pm 5%). All experimental procedures were performed in compliance with animal protocols approved by the Laboratory Animal Facility at the Hong Kong University of Science and Technology.

Constructs and peptides

DNA fragments encoding mouse MAGI-2 (UniProtKB: Q9WVQ1), mouse β -catenin (UniProtKB: Q02248) and mouse N-cadherin (UniProtKB: P15116) were amplified by the standard PCR method and inserted into a modified pET-32a vector with an N-terminal Trx-His $_6$ tag and an HRV-3C protease cleavage site. The plasmids for expressing PSD-95, Stg_CT and SAPAP are from previous studies 17,68 . The plasmids containing (SUMO) $_{10}$ and (SIM) $_{10}$ were obtained from Addgene (126948 and 126946, respectively). All constructs were confirmed by DNA sequencing. Two peptides, Stg_CT_20aa and a phosphorylated GKAP peptide, were commercially synthesized by ChinaPeptides with purity > 95%.

Protein expression and purification

All proteins were expressed in *E. coli* BL21(DE3) cells in LB medium at 37 °C until the optical density at 600 nm reached -0.6. Protein expression was induced by adding 0.25 mM IPTG at a lower culture temperature (20 °C for full-length MAGI-2 and 16 °C for remaining proteins) overnight. Recombinant proteins were purified with a Ni²+-NTA affinity column (GE Healthcare) followed by size-exclusion chromatography (SEC; Superdex 75 26/60 for Stg_Ct and Superdex 200 for all other proteins). The affinity tag of each protein was cleaved by HRV-3C protease at 4 °C overnight and removed by another step of Superdex 200 26/60 or Superdex S75 SEC with a buffer containing 50 mM Tris pH 8.2, 200 mM NaCl, 1 mM EDTA and 1 mM DTT. A final Mono Q anion-exchange chromatography step was used to remove remaining nucleic acid contaminations from full-length MAGI-2. (SUMO)₁₀, (SIM)₁₀ and PDZO-GK-(SIM)₁₀ were purified according to methods described previously⁷⁵.

Protein labeling with the fluorophores

For amide labeling, the fluorophores, including iFluor 405/Cy3/Cy5 NHS ester (AAT Bioquest) and Alexa Fluor 488/647 NHS ester (Thermo Fisher), were dissolved in DMSO. Purified proteins were exchanged into a buffer containing 20 mM HEPES pH 8.3, 200 mM NaCl, 1 mM EDTA and 1 mM DTT using a Hi-Trap desalting column. A fluorophore was added into the protein solution in a 1:1 molar ratio at a typical protein concentration of 100 μ M. Because of its limited solubility, the typical protein concentration of MAGI-2 used in dye labeling was 20 μ M and the mixture was incubated at room temperate for 1 h. The reaction was quenched by 200 mM Tris pH 8.2 and the protein in each reaction mixture was separated from the reaction dye using a desalting column with a column buffer containing 50 mM Tris pH 8.2, 200 mM NaCl, 1 mM EDTA and 1 mM DTT. The fluorescence labeling efficiency of each protein was determined by a Nanodrop 2000 (Thermo Fisher).

In vitro CaMKII \alpha-mediated SAPAP phosphorylation

The purified CaMKIIα kinase domain was activated with a tenfold ratio of calmodulin in a buffer containing 50 mM Tris pH 8.2, 100 mM NaCl, 2 mM DTT, 2 mM CaCl₂, 10 mM MgCl₂ and 1 mM ATP for 20 min at room

temperature. The activated CaMKII α was mixed with GKAP in a 1:40 molar ratio in a buffer containing 50 mM Tris pH 8.2, 100 mM NaCl, 1 mM DTT, 2 mM CaCl₂, 10 mM MgCl₂ and 1 mM ATP and the reaction mixture was incubated overnight at room temperature. Phosphorylated SAPAP was separated from CaMKII α by SEC (Superdex 75) using a column buffer containing 50 mM Tris pH 7.5, 100 mM NaCl, 1 mM EDTA and 1 mM DTT.

Sedimentation-based phase separation assay

All purified proteins were centrifuged at 16,873g at 4 °C for 10 min to remove possible precipitations before sedimentation-based phase separation assays. Proteins were directly mixed at specified concentrations. The final buffer of the sedimentation assay was 50 mM Tris pH 8.2, 100 mM NaCl, 1 mM EDTA and 5 mM DTT, unless otherwise indicated. For sedimentation-based assays, the total volume of each mixture was 50 μ l. After incubating for 10 min at room temperature, each mixture was centrifuged at 16,873g at 22 °C for 10 min. The supernatant was removed and the pellet was resuspended with 50 μ l of the same assay buffer. Proteins recovered in the supernatant and pellet fractions were analyzed by SDS-PAGE with Coomassie blue R250 staining. The intensity of each protein band on SDS-PAGE gel was quantified by ImageJ.

Imaging-based phase separation assay

All purified proteins were centrifuged at 16,873g at 4 °C for 10 min to remove precipitations before the microscope-based assays. Proteins were simultaneously directly mixed at specified concentrations. Each mixture was injected into an in-house chamber composed of a coverslip and a glass slide assembled with one layer of double-sided tape¹⁶. DIC and fluorescent images were captured using a Nikon Ni-U upright fluorescence microscope (with a ×60 oil lens) at room temperature or a Zeiss LSM 980 confocal microscope using Zeiss Zen software at 22 °C with a ×63 oil lens. Images were processed with ImageJ. For all the experiments in the absence of (SUMO)₁₀ or (SIM)₁₀, the purified proteins were mixed in the following order: Stg CT or GluN2B, PSD-95, pSAPAP, Shank, Homer, MAGI-2, β-catenin and N-cadherin. (SUMO)₁₀ or (SIM)₁₀ and MAGI-2 or Stg_CT were mixed separately in two PCR tubes and then combined together. (SUMO)₁₀ or PDZO-GK-(SIM)₁₀ was mixed with pSAPAP and then combined with MAGI-2 or Stg CT in the same manner.

ITC assay

ITC experiments were performed on a MicroCal VP-ITC calorimeter (Malvern) at 25 °C. All proteins or peptides used in this experiment were exchanged to a buffer containing 50 mM Tris pH 8.2, 100 mM NaCl, 1 mM EDTA and 1 mM DTT. Each titration point was performed by injecting a 10- μ l aliquot of one protein in the syringe into the cell containing its binding protein. The concentrations of the proteins are indicated in the figures containing each ITC curve. The titration data were fitted with the one-site binding model using Origin 7.0 (Malvern).

SEC coupled with multiangle light scattering

The SEC coupled with multiangle light scattering (SEC–MALS) system was composed of a static light scattering detector (miniDAWN, Wyatt), a differential refractive index detector (Optilab, Wyatt) and an AKTA purifier (GE Healthcare). First, $100~\mu l$ of sample was injected into a Superdex 200 Increase 10/300~GL column pre-equilibrated with a column buffer containing 50 mM Tris pH 8.2, 100~mM NaCl, 1~mM EDTA and 2~mM DTT. Data were analyzed by the ASTRA (Wyatt) software.

PSD fractionation and Immunoblotting

One brain from an 8-week-old male mouse (C57BL) was homogenized with 9 ml of buffer containing 0.32 M sucrose, 10 mM HEPES, pH 7.4, 1 mM EDTA, 1 mM EGTA, protease inhibitor cocktail (MCE, HY-K0010) and phosphatase inhibitor cocktail (UElandy, P6164) and centrifuged at

800g for 10 min at 4 °C. The recovered supernatant was centrifuged at 15.000g for 20 min at 4 °C. The pellet (Synaptosome) was resuspended with 4 ml of cold double-distilled H₂O supplied with 4 mM HEPES pH 7.4, incubated at 4 °C for 30 min and centrifuged at 25,000 g for 20 min at 4 °C. The recovered pellet (synaptic membranes) was further resuspended in 2 ml of buffer with 50 mM HEPES pH 7.4, then mixed with 2 ml of 1% Triton X-100 and incubated for 15 min at 4 °C. The mixture was centrifuged at 32,000g for 20 min at 4 °C to yield PSD in the pellet fraction. Samples were separated by 8% SDS-PAGE. Proteins were transferred to a PVDF membrane and probed with anti-PSD-95 (Abcam, ab18258:1:1.000). anti-MAGI-2 (Santa Cruz Biotechnology, sc-517008: 1:400), anti-GluN2B (Abcam, ab93610; 1:1,000), anti-GluA1 (Millipore, MAB2263, clone RH95; 1:1000), anti-β-catenin (BD Biosciences, 610154: 1:500) and anti-SAPAP1 (Thermo Fisher, PA5-78658: 1:2.000). The secondary antibodies, horseradish peroxidase (HRP)-conjugated goat anti-mouse antibody (Immunoway, RS0001; 1:20,000) and HRP-conjugated alpaca anti-rabbit IGG FC (Huabio, HA1031; 1:50,000), were used with consideration of species compatibility.

Primary hippocampal neuron culture

Rat (Sprague-Dawley) hippocampal neuronal cultures were dissected from embryonic day 19 rats and were seeded on poly(D-lysine)-coated confocal imaging dishes for direct STORM (dSTORM) imaging. The primary neurons were seeded with a density of 0.8×10^5 cells per well. The cells were plated in neurobasal medium (Gibco) containing 50 mg ml streptomycin, 50 U per ml penicillin and 2 mM GlutaMax supplemented with 2% B27 (Gibco) and 5% FBS. At 7 days in vitro (DIV7), 5 mM FdU was added to the medium to inhibit glial cell proliferation. At DIV17, the knockdown and rescue plasmids were transfected into neurons using Lipofectamine 2000 (Invitrogen) following the user's manual. The cell medium was changed in a half-volume manner with neurobasal medium containing 2% B27 and 2 mM GlutaMax twice a week.

Immunocytochemistry

Typically, transfected cells were fixed at DIV22 with 4% paraformaldehyde and 4% sucrose for 12–15 min and then washed with PBS three times, 5 min each time. After fixation, cells were blocked, permeated by the buffer containing 10% normal Donker serum (NDS) and 0.2% Triton X-100 in PBS for 1 h and washed with PBS. After washing, cells were incubated with diluted primary antibodies anti-PSD-95 (Milipore, MAB1596, clone 6G6-1C9:1:1.000), anti-pan Shank (Biolegend, 851902; 1:1,000), anti-Homer 1 (SYSY, 160003; 1:1,000) and anti-Flag antibody (Millipore, F7425, 1:400) in PBS with 3% NDS and 0.2% Triton X-100 for 1 hat room temperature. After washing with PBS three times, cells were incubated with anti-mouse Alexa 647-conjugated secondary antibody (Thermo Fisher, A31571; 1:500) and CF568-conjugated secondary antibody (Biotium, 20801; 1:1,000) in PBS with 3% NDS and 0.2% Triton X-100 for 1 hat room temperature. After washing away the free secondary antibodies with PBS for three times, dishes for dSTORM imaging were kept in PBS at 4 °C for less than 5 days.

dSTORM imaging for cultured neurons

Before dSTORM imaging, the fixed neurons were exchanged into a freshly prepared imaging buffer containing 5% D-flucose, $5.6 \mu g$ ml $^{-1}$ glucose oxidase, $40 \mu g$ ml $^{-1}$ catalase and 150 mM 2-mercaptoethanol. Imaging of each sample was completed within 1 h upon the addition of the imaging buffer. A Zeiss Elyra7 microscope with a $\times 63$ (numerical aperture = 1.4) oil objective lens was used to capture the dual-channel images. A wide-field image was captured first with 2% of the full power (500 mW) of the 488-nm, 561-nm and 647-nm laser. dSTORM images were acquired under 100% of the full power of the 561-nm and 647-nm laser with the HILO mode illumination under SMLM mode and a TIRF-hp filter was used during imaging. All images were captured with 12,000 frames with an exposure time of 30 ms per frame. Autofocus with the 'definite focus' strategy was performed at every 300 frames. Alignment

of dual channels was performed before imaging. Drift correction was performed after imaging with Zeiss's model-based autocorrelation algorithm under adjust mode. The maximum point spread function was set at 9 and signal-to-noise ratio was set at 6 when capturing single-molecule images with Zeiss Elyra7 using Zeiss Zen (black edition) software.

Quantification of dSTORM imaging for cultured neurons

Synapses were first manually tagged with the wide-field image. The cluster of super-resolution localizations in synapses was then selected manually with the help of tessellation-based autoclustering algorithm 76,77 . Masks of spine or shaft boundaries were generated by the wide-field GFP signal with manually set thresholds. An overlap coefficient was introduced to quantitatively compare the molecule distributions captured by dSTORM imaging. Two pixelated (pixel size of 20 nm \times 20 nm) two-dimensional localization density maps were calculated with the selected localizations for each channel. The density maps were then normalized with the total number of localizations of each channel. The overlap coefficient was defined as the summary of the overlapping value of each pixel between two normalized density maps. This overlap coefficient is affected only by the two normalized density distributions and has only one number to describe the degree of overlap between two distributions.

Reporting summary

Further information on research design is available in the Nature Portfolio Reporting Summary linked to this article.

Data availability

All data needed to evaluate the conclusions in the paper are present in the paper and/or Supplementary Information. Source data are provided with this paper.

Code availability

A customized script for SMT data analysis was coded with MAT-LAB, sourced from GitHub (https://github.com/NeoLShen/Code-for-phase-simulation-and-HMM-analysis). A customized script for two-dimensional and three-dimensional STORM data analysis was coded in MATLAB, sourced from GitHub (https://github.com/NeoLShen/3D-STORM-data-process-with-MATLAB-app). Details of the codes were described in previous studies^{69,71}.

References

- Levet, F. et al. SR-Tesseler: a method to segment and quantify localization-based super-resolution microscopy data. *Nat. Methods* 12, 1065–1071 (2015).
- 77. Levet, F. et al. A tessellation-based colocalization analysis approach for single-molecule localization microscopy. *Nat. Commun.* **10**, 2379 (2019).

Acknowledgements

This work was supported by grants from the National Natural Science Foundation of China (82188101), Key Area Research and Development Program of Guangdong Province (2023B0303010001), Shenzhen Bay Laboratory (S201101002), Shenzhen Talent Program (KQTD20210811090115021), Shenzhen Science and Technology Basic Research Program (JCYJ20220818100215033), Shenzhen Science and Technology Program (ZDSYS20220402111000001), Guangdong Innovative and Entrepreneurial Research Team Program (2021ZT09Y104) and Shenzhen Medical Research Fund (B2302039) to M.Z.

Author contributions

Y.C. and C.M. performed all phase separation and biochemical experiments with help from B.J., Z.S. and Y.C. performed SMT

experiments, S.C. completed PSD fractionation studies, S.Z. contributed to the PSD-95.FingR experiment. All authors analyzed the data. M.Z. drafted the paper with input from Y.C. and C.M. All authors commented on the paper. S.D. and M.Z. supervised the research. M.Z. coordinated the project.

Competing interests

The authors declare no competing interests.

Additional information

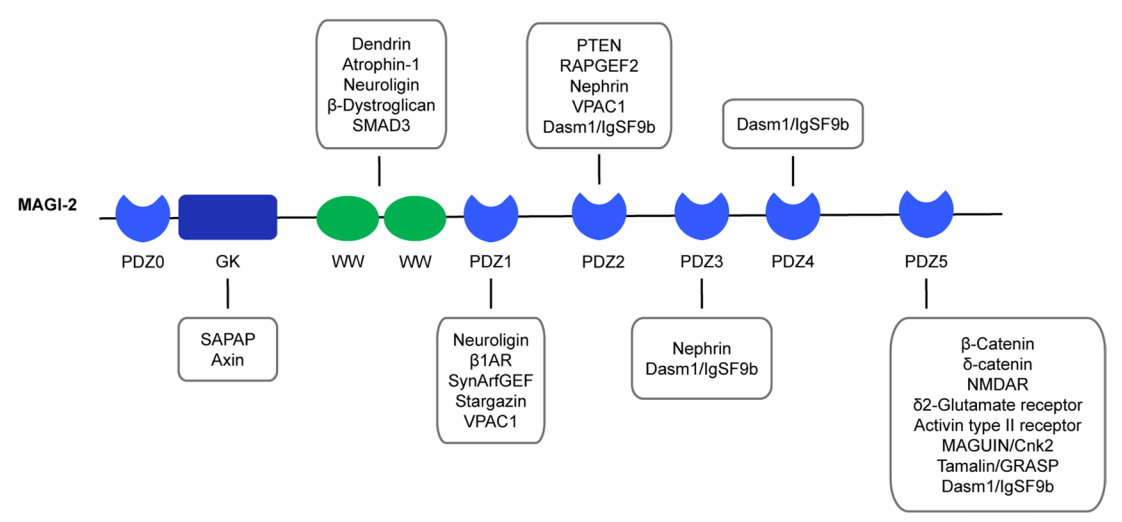
Extended data is available for this paper at https://doi.org/10.1038/s41589-025-01925-0.

Supplementary information The online version contains supplementary material available at https://doi.org/10.1038/s41589-025-01925-0.

Correspondence and requests for materials should be addressed to Mingjie Zhang.

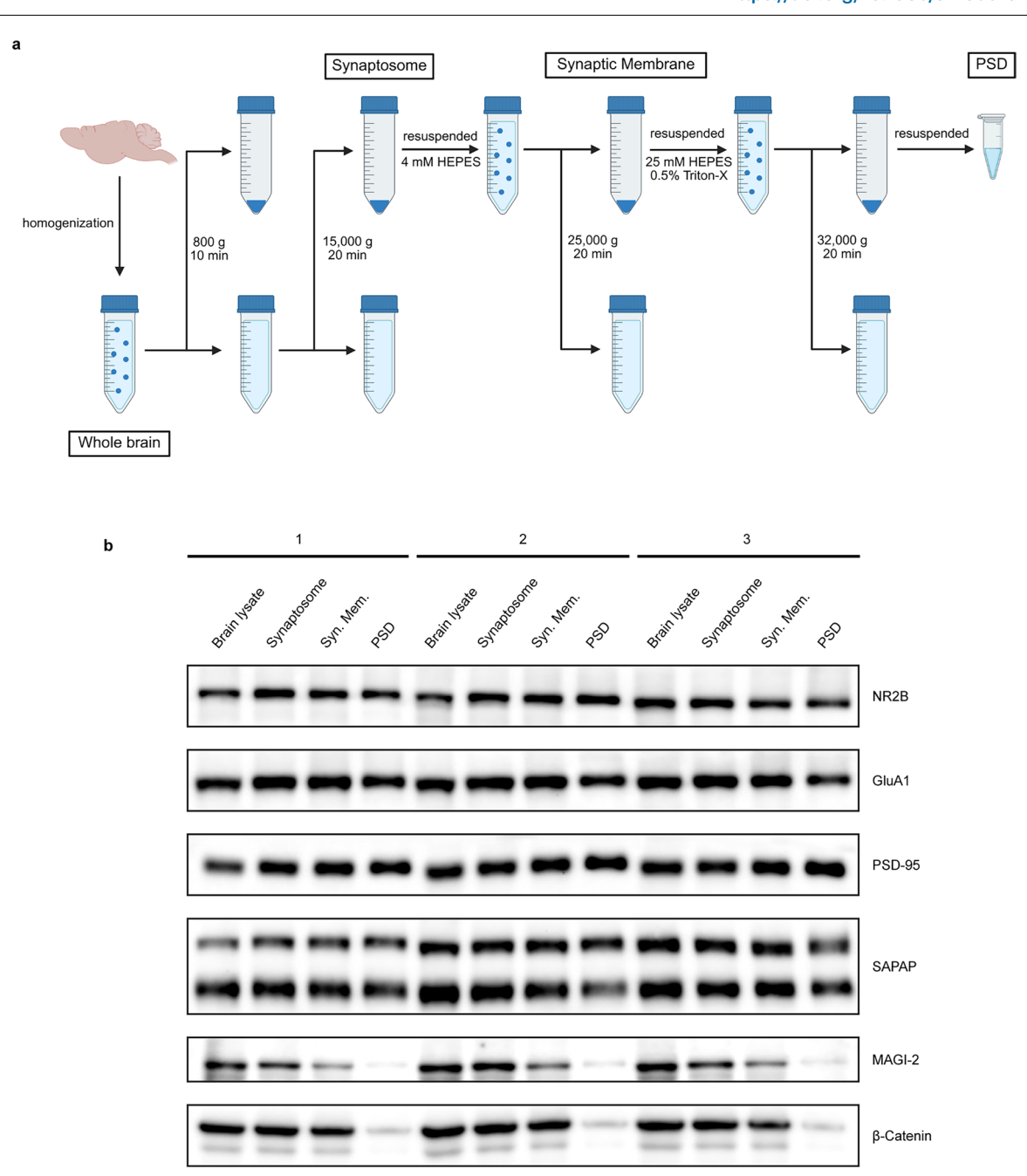
Peer review information *Nature Chemical Biology* thanks Boxun Lu and the other, anonymous, reviewer(s) for their contribution to the peer review of this work.

Reprints and permissions information is available at www.nature.com/reprints.

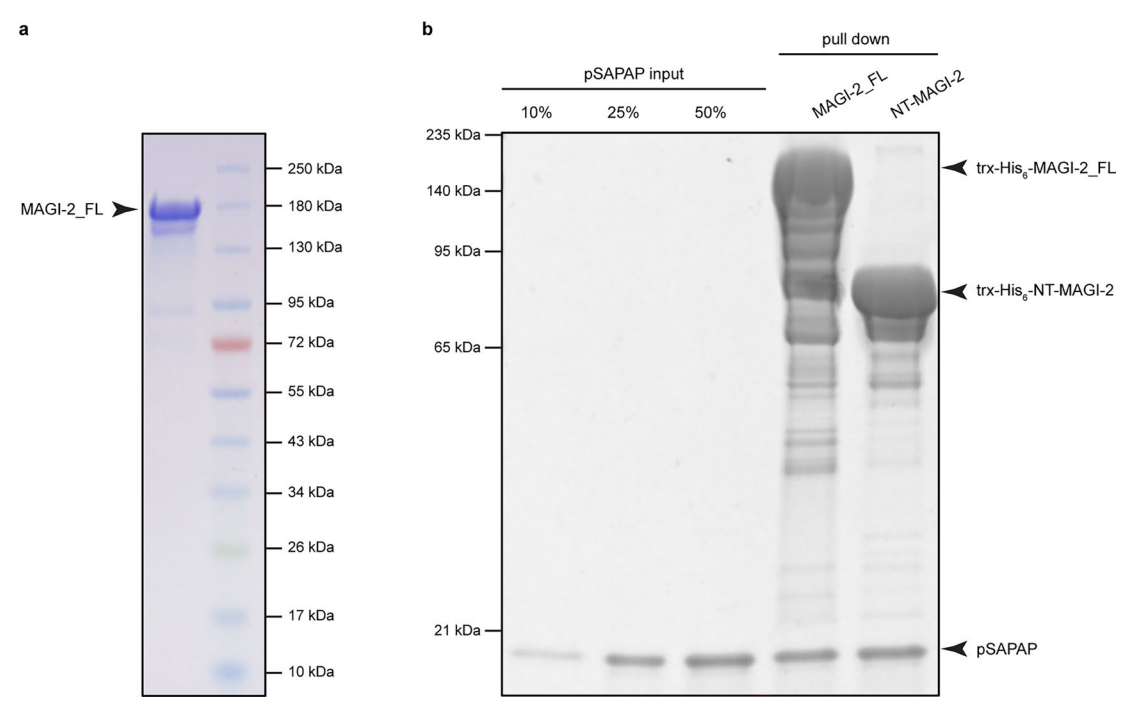


Extended Data Fig. 1| **The Domain organization and reported binding partners of MAGI-2.** Schematic diagrams of the domain organization and binding partners of MAGI-2 protein. MAGI-2 contains six PDZ domains, but only PDZ1 to PDZ5 are canonical PDZ domains with biochemical binding ability. Due to the mutation in the GLGF groove, PDZ0 does not bind to PDZ binding motif

(PBM). The crystal structure shows PDZO facilitates the GK domain folding. The GK domain is responsible for GKAP/SAPAP binding in the synapse. WW domains bind to a specific sequence called 'PY-Motif'. PDZ domains interacts with PBM (PDZ-binding motif).



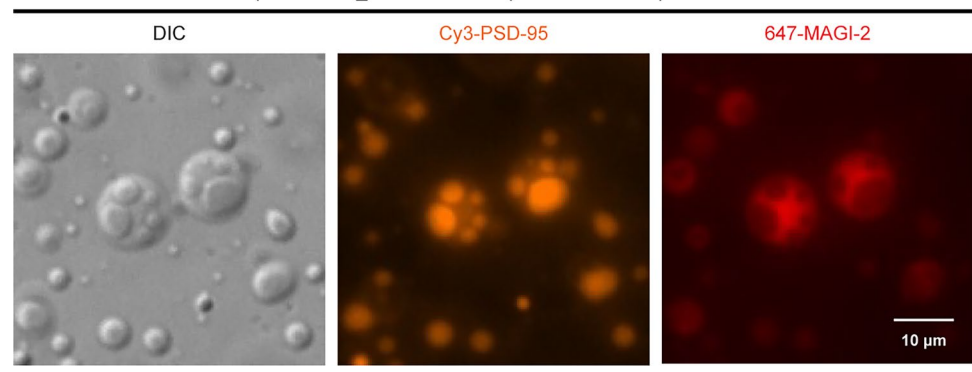
 $\textbf{Extended Data Fig. 2} | \textbf{The PSD fractionation process and immunoblotting results. (a)} \ Schematic diagrams of the PSD fractionation process. Created in BioRender. Chan, J. (2025) <math display="block"> \textbf{https://BioRender.com/tzg|z2w. (b)} \ Immunoblotting results of 3 independent PSD fractionation repeats quantified in Fig. 1c.$



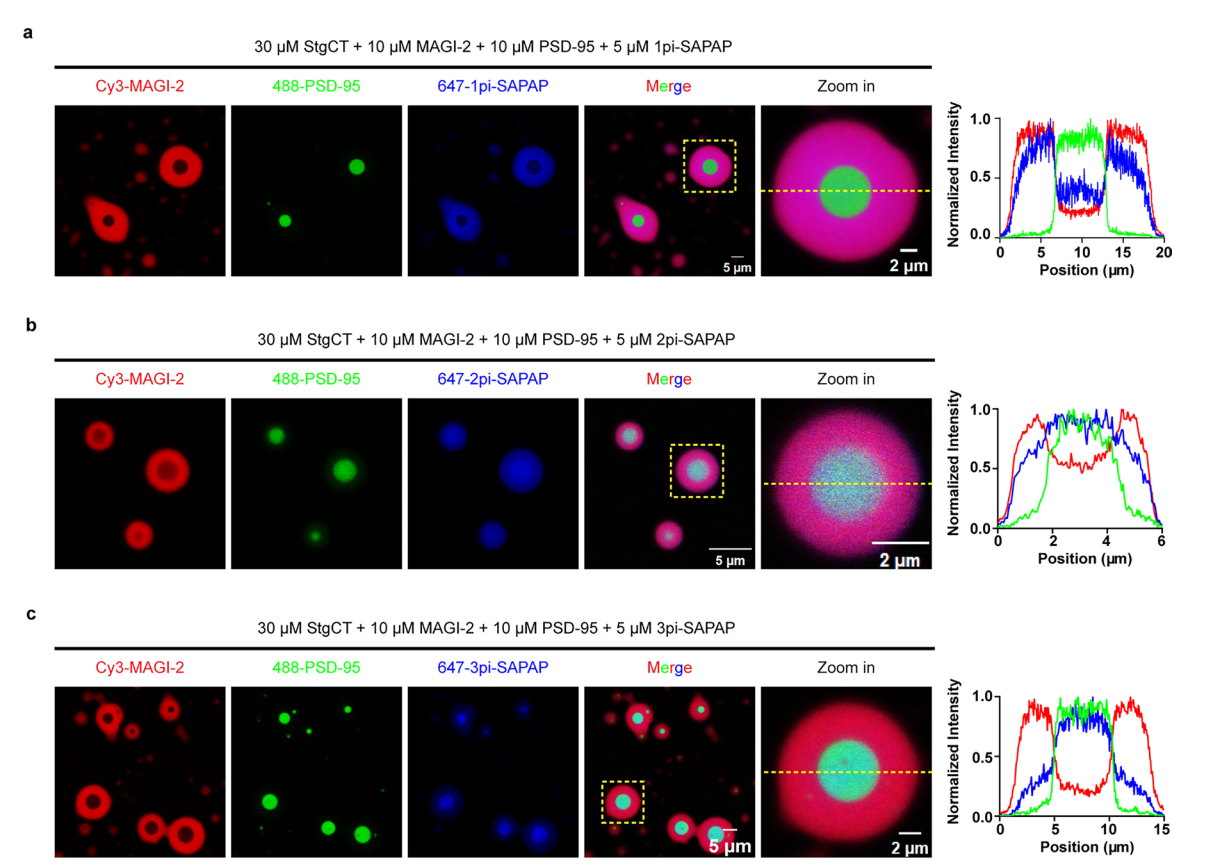
Extended Data Fig. 3 | pSAPAP binds to full-length MAGI-2 and NT-MAGI-2 with comparable affinities. (a) SDS-PAGE with Coomassie blue staining showing the quality of purified full-length MAGI-2. The protein was purified more than 6 times independently with the same quality. (b) Purified trx-His $_{\circ}$ tagged full-length

MAGI-2 and NT-MAGI-2 were used to pull down phosphorylated SAPAP and the proteins were detected by SDS-PAGE with Coomassie blue staining. The experiment was repeated 3 times with the same results.

30 μM GluN2B_1170-1482 + 10 μM MAGI-2 + 10 μM PSD-95

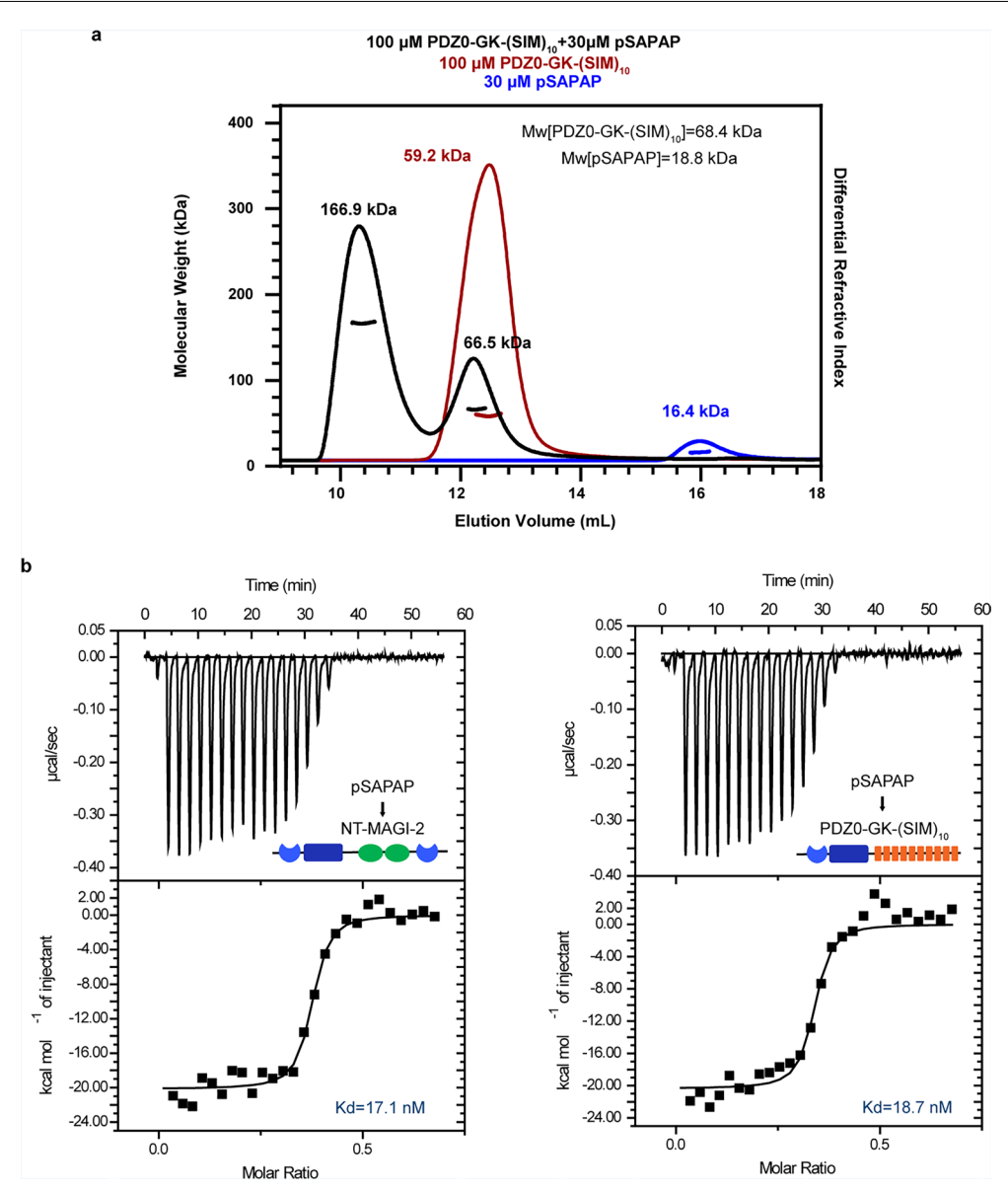


Extended Data Fig. 4 | **GluN2B formed immiscible condensates with MAGI-2 and PSD-95.** Differential interference contrast and fluorescence microscopy imaging of the condensates formed by mixing 10 μ M MAGI-2, 10 μ M PSD-95, and 30 μ M NR2B (amino acids 1170-1482). The experiment was repeated 3 times independently with the same results.



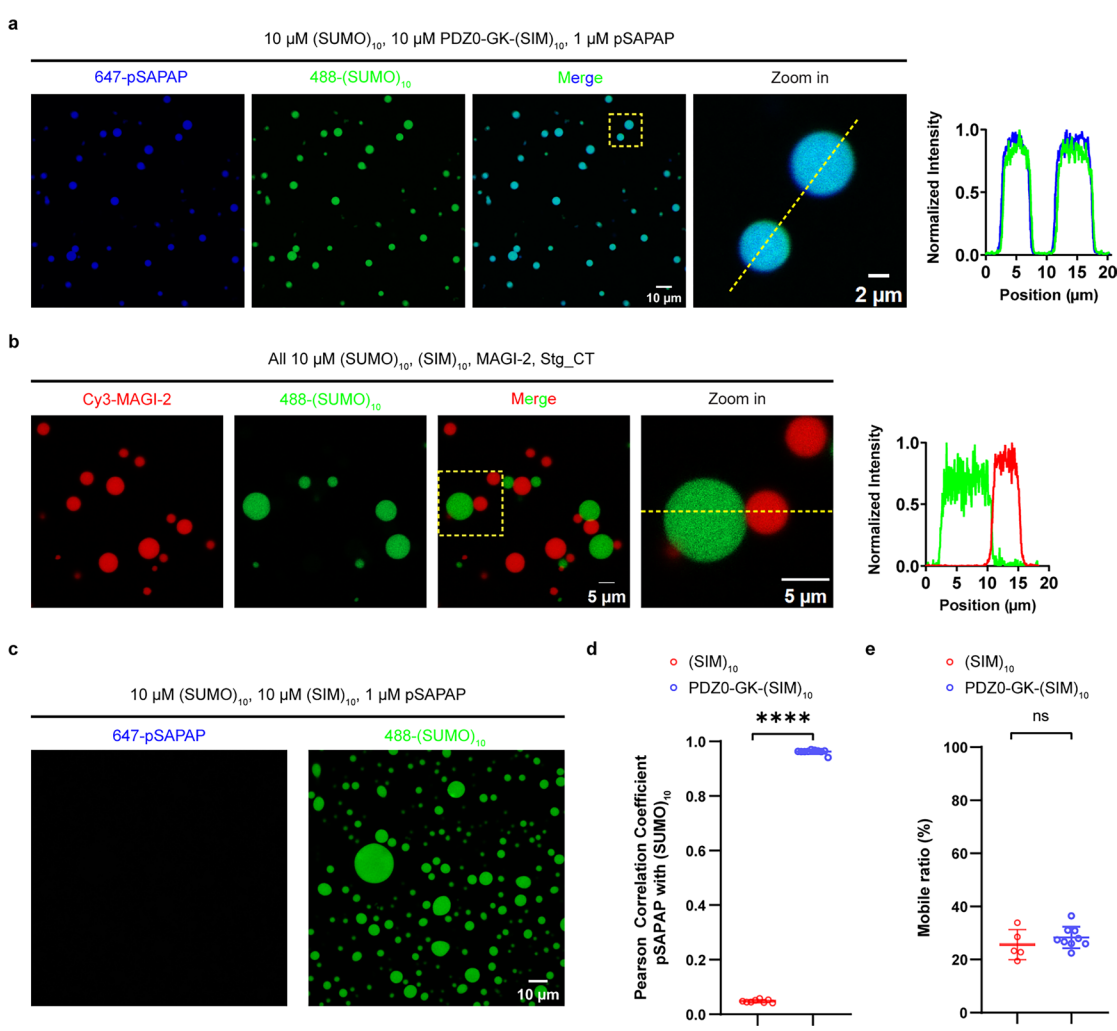
Extended Data Fig. 5 | The number of SAPAP phosphorylation affect its distribution in immiscible condensates. (a) 1pi-SAPAP was enriched in the MAGI-2 organized outer condensate in the immiscible condensates formed by 10 μ M MAGI-2, 10 μ M PSD-95, 30 μ M Stg_CT, and 5 μ M 1pi-pSAPAP. The right panel shows a line scanning analysis of the corresponding protein in the selected droplet. (b) 2pi-SAPAP was enriched in the PSD-95 organized inner condensate in the immiscible condensates formed by 10 μ M MAGI-2, 10 μ M PSD-95, 30 μ M Stg_CT, and 5 μ M 2pi-pSAPAP. Nonetheless, the MAGI-2 phase also cantained

significant amount of 2pi-pSAPAP. The right panel shows a line scanning analysis of the corresponding protein in the selected droplet. (c) 3pi-SAPAP was strongly enriched in the PSD-95 organized inner condensate in the immiscible condensates formed by 10 μ M MAGI-2, 10 μ M PSD-95, 30 μ M Stg_CT, and 5 μ M 3pi-pSAPAP. The right panel shows a line scanning analysis of the corresponding protein in the selected droplet. The experiment in this figure was repeated 3 times independently with the same results.



Extended Data Fig. 6 | pSAPAP binds to NT-MAGI-2 and PDZ0-GK-(SIM) $_{10}$ with the same affinities. (a) SEC-MALS (size-exclusion chromatography–multiangle light scattering) assay showing that PDZ0-GK-(SIM) $_{10}$ formed a stable complex with pSAPAP. (b) ITC-based assays showing that pSAPAP binds to NT-MAGI-2

(K_d ~17 nM) with the same affinity as PDZ0-GK-(SIM) $_{10}$ (k_d ~18 nM). In these experiments, 50 μ M pSAPAP was titrated into 15 μ M NT-MAGI-2 or 15 μ M PDZ0-GK-(SIM) $_{10}$.



Extended Data Fig. 7 | **PDZ0-GK-(SIM)**₁₀ - (**SUMO)**₁₀ **condensate can enrich pSAPAP.** (a) pSAPAP was enriched in the PDZ0-GK-(SIM)₁₀ – (SUMO)₁₀ condensates. The right panel is a line scanning analysis of the corresponding proteins in the selected droplet. (b) (SIM)₁₀ – (SUMO)₁₀ condensate was immiscible with MAGI-2/Stg_CT condensate. The right panel shows a line scanning analysis of the corresponding proteins in the selected droplet. (c) pSAPAP was not enriched in the (SIM)₁₀ – (SUMO)₁₀ condensate. (d) Quantification of the Pearson correlation coefficient (PCC) values between pSAPAP and

 $\begin{array}{l} (SUMO)_{10} \ in \ Panels \ \textbf{a} \ and \ \textbf{b}. \ Data \ represent \ mean \ values \pm s.d. \ (For \ (SIM)_{10} - (SUMO)_{10} \ condensate, n = 8 \ individual \ image \ fields; \ for \ PDZ0\text{-}GK\text{-}(SIM)_{10} - (SUMO)_{10} \ condensate, n = 10 \ individual \ image \ fields). \ Two-tailed t test \ was \ used, \\ ^{****P} < 0.0001. \ (\textbf{e}) \ Quantification \ of \ the \ mobile \ fractions \ of \ the \ condensates \\ formed \ by \ PDZ0\text{-}GK\text{-}(SIM)_{10}\text{-}(SUMO)_{10} \ and \ (SIM)_{10}\text{-}(SUMO)_{10}. \ A \ total \ of \ 4063 \\ and \ 2644 \ trajectories \ for \ PDZ0\text{-}GK\text{-}(SIM)_{10} \ and \ (SIM)_{10} \ from \ 3 \ and \ 5 \ individual \\ experiments, \ respectively, \ were \ used \ to \ perform \ this \ quantification. \ Data \\ represent \ mean \ values \ \pm \ s.d. \ Two-tailed \ t \ test \ was \ used, \ P = 0.3102. \end{array}$

nature portfolio

Corresponding author(s):	Mingjie Zhang
Last updated by author(s):	Apr 8, 2025

Reporting Summary

Nature Portfolio wishes to improve the reproducibility of the work that we publish. This form provides structure for consistency and transparency in reporting. For further information on Nature Portfolio policies, see our <u>Editorial Policies</u> and the <u>Editorial Policy Checklist</u>.

\sim				
<.	tat	ŀις	11	\sim

For	all statistical analyses, confirm that the following items are present in the figure legend, table legend, main text, or Methods section.
n/a	Confirmed
	The exact sample size (n) for each experimental group/condition, given as a discrete number and unit of measurement
	A statement on whether measurements were taken from distinct samples or whether the same sample was measured repeatedly
	The statistical test(s) used AND whether they are one- or two-sided Only common tests should be described solely by name; describe more complex techniques in the Methods section.
\boxtimes	A description of all covariates tested
\boxtimes	A description of any assumptions or corrections, such as tests of normality and adjustment for multiple comparisons
	A full description of the statistical parameters including central tendency (e.g. means) or other basic estimates (e.g. regression coefficient) AND variation (e.g. standard deviation) or associated estimates of uncertainty (e.g. confidence intervals)
	For null hypothesis testing, the test statistic (e.g. <i>F</i> , <i>t</i> , <i>r</i>) with confidence intervals, effect sizes, degrees of freedom and <i>P</i> value noted <i>Give P values as exact values whenever suitable.</i>
\boxtimes	For Bayesian analysis, information on the choice of priors and Markov chain Monte Carlo settings
\boxtimes	For hierarchical and complex designs, identification of the appropriate level for tests and full reporting of outcomes
\boxtimes	Estimates of effect sizes (e.g. Cohen's d, Pearson's r), indicating how they were calculated
	Our web collection on statistics for biologists contains articles on many of the points above.

Software and code

Policy information about availability of computer code

Data collection

The ZEISS Zen (black edition) was used for Confocal and STORM imaging. ASTRA 8.1.1 was used for SEC-MALS (size-exclusion chromatography–multiangle light scattering) data collection. Isothermal titration calorimetry was performed using MicroCal VP-ITC.

Data analysis

A customized script for single molecule tracking was coded with MATLAB 2024a, the source were released at GitHub: https://github.com/NeoLShen/Code-for-phase-simulation-and-HMM-analysis. A customized script for 3D STORM data analysis was coded with MATLAB, the source were released at GitHub: https://github.com/NeoLShen/3D-STORM-data-process-with-MATLAB-app. These codes were described in our earlier publications (refs 68, 69 of the paper). The Origin 7 and GraphPad Prism 8 was used for statistical analysis. The software ImageJ was used for analysis of the fluorescence intensity of the condensates.

For manuscripts utilizing custom algorithms or software that are central to the research but not yet described in published literature, software must be made available to editors and reviewers. We strongly encourage code deposition in a community repository (e.g. GitHub). See the Nature Portfolio guidelines for submitting code & software for further information.

Data

Policy information about availability of data

All manuscripts must include a data availability statement. This statement should provide the following information, where applicable:

- Accession codes, unique identifiers, or web links for publicly available datasets
- A description of any restrictions on data availability
- For clinical datasets or third party data, please ensure that the statement adheres to our policy

All data needed to evaluate the conclusions in the paper are present in the paper and/or Supplementary Information.

Research involving human participants, their data, or biological material

Policy information about studies with <u>human participants or human data</u>. See also policy information about <u>sex, gender (identity/presentation)</u>, <u>and sexual orientation</u> and <u>race, ethnicity and racism</u>.

Reporting on sex and gender	N/A
Reporting on race, ethnicity, or other socially relevant groupings	N/A
Population characteristics	N/A
Recruitment	N/A
Ethics oversight	N/A

Note that full information on the approval of the study protocol must also be provided in the manuscript.

Field-specific reporting

Please select the one below that	is the best fit for your i	research. If you are n	ot sure, read the appro	priate sections before n	naking your selection.

Life sciences Behavioural & social sciences Ecological, evolutionary & environmental sciences

 $For a \ reference \ copy \ of the \ document \ with \ all \ sections, see \ \underline{nature.com/documents/nr-reporting-summary-flat.pdf}$

Life sciences study design

All studies must disclose on these points even when the disclosure is negative.

Sample size

We did not compute statistical analyses to predetermine sample sizes. Sample sizes were chosen based on similar published studies in the literature (refs 68, 71 of the paper). All analyzes were at least two and more independent samples (for n, see figure legends), and in each experimental repeat yielding highly similar results.

Data exclusions

No data were excluded

Our results were successfully validated in >3 repetitions, and all experimental findings were reliable reproduced.

Randomization

Randomization was performed for choosing the imaging fields.

Blinding To ensure blinding, the STORM image acquisition and data processing were performed by different authors.

Reporting for specific materials, systems and methods

We require information from authors about some types of materials, experimental systems and methods used in many studies. Here, indicate whether each material, system or method listed is relevant to your study. If you are not sure if a list item applies to your research, read the appropriate section before selecting a response.

₽	
$^{\circ}$	
≓	
$\overline{}$	
N.	

Materials & experime	ntal systems Methods	
n/a Involved in the study	n/a Involve	d in the study
Antibodies	⊠ ☐ ChI	P-seq
Eukaryotic cell lines	∑	v cytometry
Palaeontology and a	rchaeology 🔀 🔲 MR	-based neuroimaging
Animals and other o	rganisms	
Clinical data		
Dual use research o	[:] concern	
⊠ □ Plants		
I		
Antibodies		
Antibodies used	Anti-Flag antibody, Millipore, F7425	
	Anti-PSD-95 antibody, Abcam, ab18258 Anti-MAGI-2 antibody, Santa Cruz Biotechr	vology sc-517008
	Anti-NMDAR2B antibody, Abcam, ab93610	
	Anti-GluR1 antibody, Millipore, MAB2263,	
	Anti-Beta-catenin antibody, BD Biosciences Anti-SAPAP1 antibody, ThermoFisher, PAS-	
	Anti-PSD-95 antibody, Milipore, MAB1596,	clone 6G6-1C9
	Anti-Pan Shank, Biolegend, 851902 Anti-Homer1, SYSY, 160003	
	Anti-Flag antibody, Millipore, F7425	
	HRP-conjugated goat anti-mouse antibody HRP-conjugated alpaca anti-rabbit IGG FC,	
	Anti-Mouse Alexa647-conjugated seconda	
	Anti-Rabbit CF568-conjugated secondary a	ntibody, Biotium,20801
Validation	Anti-Flag antibody (Millipore, F7425): Supp	lier has been validated in immunofluorescence analysis of Human HEK-293T cells over-
	expressing N or C-Terminal Flag tagged fus	·
	lysate and SHSY5Y whole cell lysate.	upplier has been validated in Western blot analysis of mouse, rat, or human brain tissue
	Anti-MAGI-2 antibody (Santa Cruz Biotechi	nology, sc-517008): Supplier has been validated in Western blot analysis of NCI-H226
	whole cell lysate. Anti-NMDAR2B antibody (Abcam, ab93610): Supplier has been validated in Western blot analysis of induced HEK-T lysate.
		clone RH95): Supplier has been validated in Western blot analysis of rat brain lysate.
		s, 610154): Supplier has been validated in Western blot analysis of Hela cell lysate78658): Supplier has been validated in Western blot analysis of mouse or rat brain tissue
	extracts.	70036). Supplier has been validated in Western blot analysis of filouse of fat brain tissue
		clone 6G6-1C9): Supplier has been validated in immunocytochemistry of PC12.
		been validated in immunostaining of a hippocampus neuron. lier has been validated in immunofluorescence human HEK-293T cells over-expressing N-
	terminal Flag tagged fusion protein.	· •
Animals and othe	r research organisms	
Policy information about <u>st</u> <u>Research</u>	udies involving animals; ARRIVE guideli	nes recommended for reporting animal research, and <u>Sex and Gender in</u>
Laboratory animals	Embryonic day 19 rat (Sprague-Dawley), A	dult 8 week mouse (C57BL)
3461 L L	No. 211 - 2 - 1 - 1 - 1 - 1 - 1 - 1 - 1	

Laboratory animals	Embryonic day 19 rat (Sprague-Dawley), Adult 8 week mouse (C57BL)	
Wild animals	No wild animals were used in the study.	
Reporting on sex	N/A	
Field-collected samples	No field collected samples were used in the study.	
Ethics oversight	All experimental procedures were performed in compliance with animal protocols approved by the Laboratory Animal Facility at the Hong Kong University of Science and Technology.	

Note that full information on the approval of the study protocol must also be provided in the manuscript.

Plants

Seed stocks	N/A
Novel plant genotypes	N/A
Authentication	N/A